Journal of Structural Geology 105 (2017) 44–61

Contents lists available at ScienceDirect

Journal of Structural Geology

journal homepage: www.elsevier.com/locate/jsg

Influence of a pre-existing basement weakness on normal fault growth during oblique extension: Insights from discrete element modeling

Chao Deng[a,*], Robert L. Gawthorpe[a], Emma Finch[b], Haakon Fossen[c,a]

[a] Department of Earth Science, University of Bergen, Allégaten 41, 5007 Bergen, Norway
[b] School of Earth Atmosphere and Environmental Science, University of Manchester, Oxford Road, Manchester M13 9PL, UK
[c] Museum of Natural History, University of Bergen, Allégaten 41, 5007 Bergen, Norway

ARTICLE INFO

Keywords:
Multiphase rifting
Fault reactivation
Fault growth
Fault interaction
Non-collinear fault

ABSTRACT

We use discrete element modeling to investigate three-dimensional fault geometry and the three-dimensional evolution of a fault network that develops above a 60° dipping planar pre-existing weakness striking 60° relative to the extension direction. The evolution of the fault network comprises three stages: (i) reactivation of pre-existing structure and nucleation of new faults (0–10% extension); (ii) radial propagation and interaction between reactivated structure and new faults (15%–20% extension); and (iii) linkage between reactivated structure and adjacent faults (20%–25% extension). During the first stage, the pre-existing structure mostly reactivates, forming a long and under-displaced fault. New faults are mainly extension-perpendicular and dip at 60°. During the second stage, 'saw-tooth' fringes grow upwards from the upper tip of the reactivated structure (which becomes the major fault) and influence the density and orientation of surrounding faults. During the third stage, the reactivated structure links laterally and vertically with adjacent faults, creating non-planar fault geometries. Following linkage, the reactivated structure enhances the displacement of linked faults along branch lines. Our study demonstrates that pre-existing weak faults can be reactivated, propagating upwards in an irregular ('saw-tooth') pattern, and affecting fault density, orientation, dip and displacement, and providing the nucleation site of new faults.

1. Introduction

Normal faults developing during a single rift phase ideally strike perpendicular to the extension direction and show approximately collinear configuration (e.g. Anderson, 1951; Gawthorpe and Leeder, 2000; Cowie et al., 2000, 2005). The general evolution of a rift-related normal fault population in homogeneous crust is commonly considered in terms of a three-stage model: (i) fault initiation, characterized by the nucleation of numerous short, small-displacement fault segments; (ii) interaction and linkage between adjacent fault segments, and; (iii) continued activity on a few large, through-going fault systems that bound half graben depocenters (e.g. Cowie et al., 2000, 2005; Gawthorpe and Leeder, 2000; McLeod et al., 2000; Meyer et al., 2002; Gawthorpe et al., 2003).

Multiphase rift basins and rifts that are built on a previously faulted or folded basement are prone to develop arrays of non-collinear faults, with interaction between reactivated and secondary faults. Examples of non-collinear fault arrays that are interpreted to result from multiphase rifting include the NW Shelf of Australia (e.g. Frankowicz and McClay, 2010), Gulf of Thailand (e.g. Morley et al., 2004, 2007), Gulf of Aden (e.g. Lepvrier et al., 2002; Bellahsen et al., 2006), the northern North Sea (e.g. Badley et al., 1988; Færseth, 1996; Færseth et al., 1997; Odinsen et al., 2000; Whipp et al., 2014; Duffy et al., 2015), and Milne Point, Alaska (Nixon et al., 2014). Nixon et al. (2014) found that second-phase faults abut against reactivated first-phase faults, and showed that two abutting faults can link kinematically by reactivating a segment of the first-phase fault. Duffy et al. (2015) found similar evidence that second-phase faults abut against or were retarded by a reactivated first-phase fault in the northern North Sea. Such observations indicate that fault evolution in a multiphase rift basin is more complicated than that predicted by the aforementioned three-stage normal fault evolution model.

Physical models greatly help us understand how non-collinear faults and fault interactions evolve during two-phase extension (e.g. McClay and White, 1995; Keep and McClay, 1997; Henza et al., 2010, 2011). Henza et al. (2011) suggested that reactivated first-phase faults can interact and link with second-phase faults to form non-collinear fault geometries with a moderately developed first-phase fault population. However, these models have difficulty in visualizing the model interior and the three-dimensional fault geometry during extension. Although

* Corresponding author.
E-mail addresses: Chao.Deng@geo.uib.no, dengchao0926@gmail.com (C. Deng).

https://doi.org/10.1016/j.jsg.2017.11.005
Received 11 July 2017; Received in revised form 7 November 2017; Accepted 8 November 2017
Available online 11 November 2017

Nixon et al. (2014) and Duffy et al. (2015) illustrated three-dimensional fault geometry and classified fault interaction styles based on final fault displacement analysis, the complete fault array is still not well understood because the 'root' of first-phase faults is deeply buried. Questions remain about the evolution of normal fault networks where reactivation of pre-existing structures influences their development. Specific questions include: i) How are pre-existing faults reactivated and how do they propagate during subsequent rifting? ii) How does a reactivated normal fault influence and interact with newly formed faults as rifting progresses? iii) How different is the normal fault geometry near a reactivated fault compared to the geometry of more distant faults? In order to answer these questions we employ a three-dimensional discrete element model to simulate crustal extension with a pre-existing planar weakness striking oblique to extension direction. The model enables us to observe three-dimensional fault geometry during extension, making it possible to analyze fault growth history and the effect of the pre-existing weakness on fault network evolution in space and time.

2. Methodology

2.1. Discrete element model

The discrete element model used in the paper simulates the crust as an assembly of spherical elements (e.g. Cundall and Strack, 1979; Mora and Place, 1993, 1994), and has been successfully used to investigate crustal deformation, such as the growth of faults (e.g., Imber et al., 2004; Hardy and Finch, 2006, 2007; Schöpfer et al., 2006, 2007a, b; Egholm et al., 2007; Hardy, 2013; Finch and Gawthorpe, 2017), folding (Finch et al., 2003, 2004; Hardy and Finch, 2005), boudinage (Komoróczi et al., 2013) and contractional wedges in mechanical stratigraphy (Wenk and Huhn, 2013). In this discrete element model, the crust consists of an upper part that deforms in a brittle manner and a lower part that behaves in a firmo-viscous way (Ranalli, 1995) (Fig. 1a–b).

In the upper crust, neighboring elements (element i and neighbor j) interact in pairs through linear elastic repulsive-attractive force (Mora and Place, 1993) (Fig. 1b), which is represented by a breakable elastic bond that follows

$$F_{ijU} = \begin{cases} K(r - r_0), & r < r_b, \ \textit{intact bond} \\ K(r - r_0), & r < r_0, \ \textit{broken bond} \\ 0, & r \geq r_0, \ \textit{broken bond} \end{cases} \quad (1)$$

In Equation (1), K is the bond stiffness (elastic constant), r is the current separation between the element pair, r_0 is the equilibrium separation and r_b is the breaking separation. r_b is normally less than $1.1r_0$ (Mora and Place, 1994). Element i experiences an attractive force through the bond with the neighbor j (i.e. $r < r_b$), but no further attractive force when the bond is broken (i.e. $r > r_b$). A broken bond is not allowed to heal, and elements experience a repulsive force when they return to a compressive contact (i.e. $r < r_0$).

In the lower crust, elements interact through linear firmo-viscous (Newtonian fluid) forces including an elastic and a linearly viscous force in parallel, representing a firmo-viscous body (Fig. 1b). The component of the elastic force is

$$F_{ijL}^{elastic} = \begin{cases} K_c(r - r_0), & r < r_0 \\ 0, & r > r_0 \end{cases} \quad (2)$$

K_c is the bond stiffness in compression, consistent with K in the upper crustal elements. And the bond between elements in the lower crust has elastic properties in compression only (i.e. $r < r_0$). The component of viscous force is

$$F_{ijL}^{viscous} = -\eta \Delta \dot{x}_{ij} \quad (3)$$

Here η is the Kelvin viscosity and determined by empirical experiments, $\Delta \dot{x}_{ij}$ is relative velocity between elements i and j.

Since the lower crust behaves like a viscous fluid, elements within it can flow out of the model at the boundaries. To prevent this, the model is constrained by boundary walls in the x- and y-component directions. These walls exert a repulsive force on any element that crosses the boundary. In that way, the model is treated as a part of a larger system of elements that have the same mechanical properties. The force, F_{iB}, due to the boundary walls is given by

$$F_{iB} = -K_B r_B. \quad (4)$$

K_B is the elastic stiffness of the boundary wall and r_B is the distance by which the element exceeds the boundary (Wenk and Huhn, 2013).

As a whole, the crust is considered an elastic-brittle-plastic plate hydrostatically floating on a fluid mantle at a specific depth, in order to reach a hydrostatic equilibrium (King et al., 1988). This depth depends on a defined ratio of the mantle and crust densities. Under this circumstance, the force due to gravity and flotation, F_{iG}, is exerted on all elements in the vertical, z-component direction and follows

$$F_{iG} = g[(\rho_m - \rho_c)V_B - \rho_c V_A]. \quad (5)$$

Here g is the gravitational acceleration, ρ_m and ρ_c are mantle and crust densities respectively, and V_A and V_B are the volumes of an element above and below the hydrostatic equilibrium. The volume of an element above the hydrostatic equilibrium experiences a downward force, whereas the volume below the hydrostatic equilibrium experiences a resultant upward force. Additionally, a damping force that allows energy to be dissipated is applied to avoid kinetic energy building up in the closed system. This artificial viscous force is used to attenuate dynamic phenomena such as reflected waves from the boundary of models, in order to keep the system less dynamic and more quasi-static (Donzé et al., 1994; Mora and Place, 1994, 1998). The damping force, F_{iD}, is

$$F_{iD} = -v \Delta \dot{x}_{ij} \quad (6)$$

Here v is the dynamic viscosity, and $\Delta \dot{x}_{ij}$ is the relative velocity between elements.

In order to reduce the cost of running a model, shear force caused by relative slip between elements is not considered within this technique as if the rock mass is frictionless (e.g., Donzé et al., 1994; Mora and Place, 1994, 1998; Hardy and Finch, 2007). Mora and Place (1994) successfully simulated the frictional stick-slip instability in a rock assemblage without shear force. Also, Finch et al. (2003, 2004) simulated normal faulting in mechanical stratigraphy above a basement structure. Previous studies suggested that realistic crustal deformation can be successfully simulated in frictionless rock mass. Therefore, the total force that an element in the upper crust experiences is

$$F_{iU}^{Total} = \sum_{j=1,n} F_{ijU} + F_{iB} + F_{iG} + F_{iD} \quad (7)$$

And the total force that an element in the lower crust experiences is

$$F_{iL}^{Total} = \sum_{j=1,n} (F_{ijL}^{elastic} + F_{ijL}^{viscous}) + F_{iB} + F_{iG} + F_{iD} \quad (8)$$

where n is the number of neighbors.

The boundary condition is implemented by imposing an external extension on all elements in the y-component direction to simulate movement of a rigid boundary wall while the opposite wall is static (Fig. 1a). The total run time is subdivided into numerous time steps, with each time step corresponding to a small increment. At each time step, elements are moving to new locations in the extension direction determined by equations of motion following Newtonian physics (Hardy and Finch, 2006). The new location of elements is:

$$Y_i(t+1) = Y_i(t) + \Delta Y \left(\frac{Y_i(t)}{Y_{\max}(t)} \right) \quad (9)$$

$Y_i\ (t+1)$ is the element location at time step $t+1$, $Y_i\ (t)$ is the element location at time step t, ΔY is the extension increment per time step and

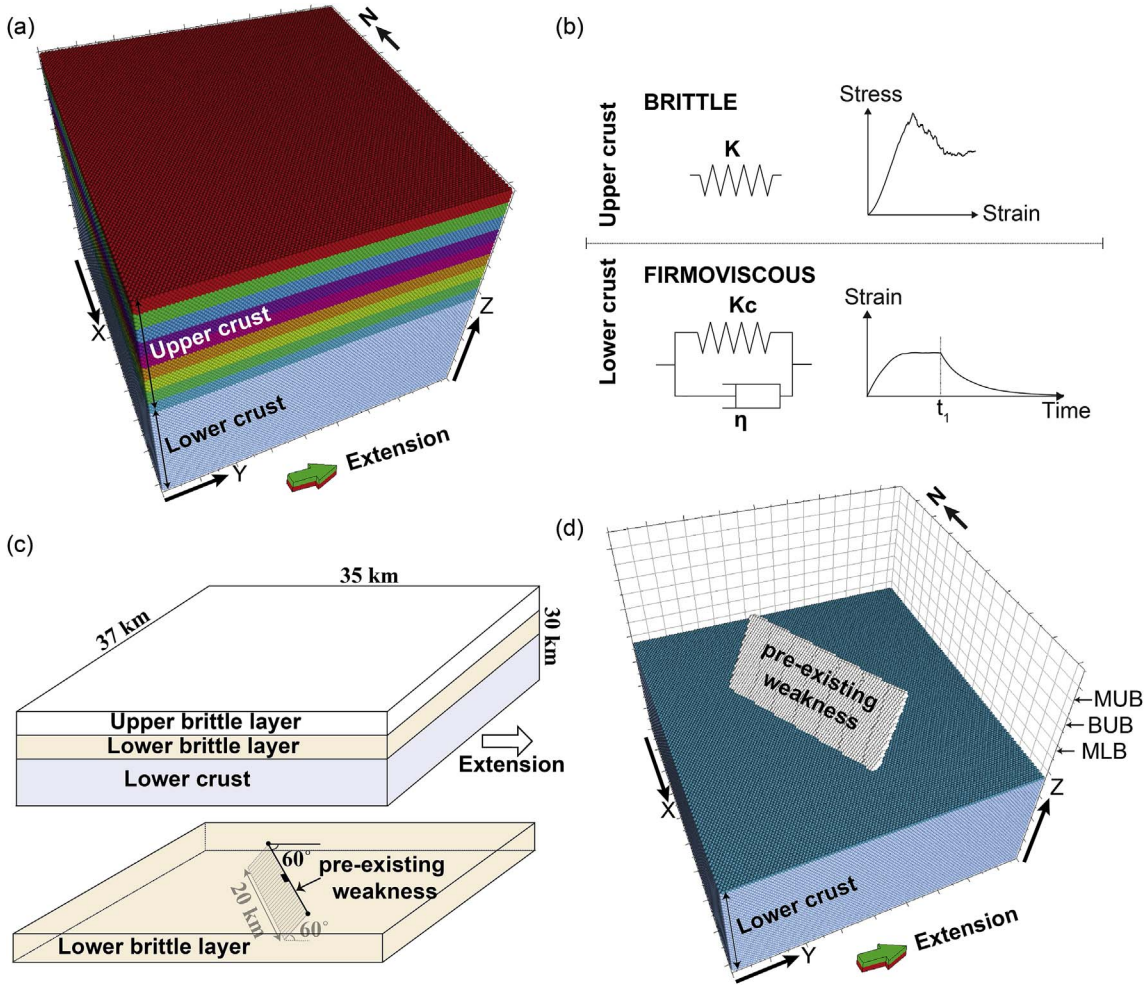

Fig. 1. Model set-up. (a) Initial set-up of the experimental media. (b) Sketch of the forces within the upper and lower crust and their rheological response. (c) Cartoon of the three-layer model; Lower figure shows the lower brittle layer with a pre-existing weakness. (d) The media from (a) highlighting the relative location of the pre-existing weakness and lower firmoviscous crust. The pre-existing weakness represents a basement structure. And the overlying brittle layer is assumed to have been deposited before the extension. MUB – middle of the upper brittle layer. BUB – bottom of the upper brittle layer. MLB – middle of the lower brittle layer.

Y_{max} *(t)* is the maximum length of the model in the extension direction at time step *t*.

Lithosphere-scale models employing the solution of thermo-mechanically coupled rheology investigated the control of temperature variations on structural style in rifts (Behn et al., 2002; Cowie et al., 2005; Huismans and Beaumont, 2007). Behn et al. (2002) observed that deformation was distributed between several sets of conjugate normal faults without a lateral temperature gradient, but localized on one major fault near the rift axis in the presence of a lateral temperature gradient. Our study aims to examine the evolution of a fault array above a pre-existing structure in fault blocks scale, thus, temperature variations through time are not considered.

2.2. Experiment set-up

We establish a regular hexagonal model consisting of 1,830,000 elements as the crust, with dimensions of 213 × 201 × 173 (x,y,z) model units (m.u.) (Fig. 1a). Horizons are initially defined as an integer value of their height (z) in model units; there are 173 horizons in total. One model unit is equivalent to 173 m, which is the radius of an element, and the model represents dimensions of 37 × 35 × 30 km (Fig. 1c). The model incorporates three layers: i) a bottom layer of 15 km thickness representing the lower crust; ii) a lower brittle layer of 7.5 km thickness representing the lower part of the upper crust or basement; and iii) an upper brittle layer of 7.5 km thickness representing the upper part of the upper crust (Fig. 1c). A pre-existing planar weakness is defined to terminate at the top and bottom of the lower brittle layer (Fig. 1c–d). The pre-existing weakness is 20 km long, dipping 60° and making a 60° strike angle between its orientation and the extension direction. Elements in the upper brittle layer are randomly assigned breaking thresholds without preferential orientation, representing undeformed sediment overlying the pre-existing weakness before extension. Table 1 shows the physical parameters for each layer; their values are comparable to rift basins in nature and many experiments scaled for investigation of fault development in rift basins. In addition, flotation is simulated by setting rock densities to be 2800 kg m^{-3} and 3300 kg m^{-3} for the crust and mantle, respectively.

Extension is implemented toward the east within the model, while the western end is fixed (Fig. 1a). Experiments are run for 50,000 time steps with data output at 1000 time step intervals, generating 50 data files. A time step is equivalent to 100 years, so the total run time is 5 Myr with an output interval of 100,000 years. This total run time is within the range of the duration for a natural rift basin, which is believed to be 1–15 Myr (Nicol et al., 1997). The rate of extension is 0.001 units per time step or 1.73 mm yr^{-1} with each data output correlating to 0.5% extension to a total of 25%. This corresponds to strain rates varying from 1.585 × 10^{-15} s^{-1} to 1.288 × 10^{-15} s^{-1} as extension progresses, which are comparable to the recorded strain rates ranging from 1.0 × 10^{-16} to 4.0 × 10^{-14} s^{-1} in rift basins (Kusznir and Park, 1987; Nicol et al., 1997).

Table 1
Rock parameters of each layer in the model.

Rock parameters		Upper crust			Lower crust
		Upper brittle layer	Lower brittle layer	Pre-existing weakness	
Element property	Elastic constant (K/K_c)	10×10^{10}	10×10^{10}	10×10^{10}	10×10^{10}
	Kelvin viscosity (η)				2.0×10^{11} Pa s
	Breaking threshold (r_b)	0.025–0.1 m.u.	0.05–0.1 m.u.	0.005–0.01 m.u.	
	Bond strength	2.5–10 GPa	5–10 GPa	0.5–1 GPa	
Assembly property	Poisson's ratio	0.25	0.25		
	Young's modulus (E)	108 GPa	108 GPa		

m.u. represents model units.

2.3. Fault analysis

A continuous alignment of elements with similar dips, heaves (horizontal offset between element pairs in the extension direction) exceeding 50 m and positive throws (vertical offset) define a fault. The heave value used has been chosen through testing and prevents fault definition including elements displaced by flexural rotation of horizons in hanging walls and footwalls (Finch and Gawthorpe, 2017). In the numerical model, the heave between an element pair in the extension direction is examined in each data output. Elements associated with faults are then extracted and stored during extension, from which the geometry, growth and interaction of individual structures are determined.

Horizons from the middle (MUB or horizon 153) and bottom (BUB or horizon 133) of the upper brittle layer, and the middle of the lower brittle layer (MLB or horizon 113) are extracted for analyzing fault length and strike at various depths (Figs. 1d and 2). Fault trace at each horizon is drawn as a line to aid visualization of the tips of each fault, permitting fault geometries in map view to be assessed. To examine fault growth and linkage, the throws (vertical offset) recorded for elements that constitute selected faults are projected onto strike sections at various stages of extension. Fault interaction styles are also investigated in three-dimensions by strike projection of throw on associated faults, thus, the location of throw maximum (T_{max}) can be determined. The value of D_{max} is then approximated by $D_{max} = 2 \times T_{max}/\sqrt{3}$, assuming that faults are generally dipping at 60°. Fault length (L) is approximated by measuring the horizontal distance from the element with the maximum x-value to that with the minimum x-value along the strike.

3. The overall fault network

At the end of extension (25%), differences are observed between fault patterns on the three selected horizons. Firstly, fault density decreases with depth, associated with the stronger bond strength in the lower brittle layer than the upper brittle layer (Fig. 2). Secondly, the major fault, F1, is related to the reactivation of the pre-existing weakness and forms a single long fault at depth, consisting of two segments (F1a and F1b in Fig. 2b–c). Segment F1a mimics the pre-existing weakness geometry, and segment F1b forms perpendicular to the extension direction. However, the upper part of fault F1 is represented by four 'saw-tooth' fringes (segments F1c to F1f) in the middle of the upper brittle layer (Fig. 2a). A rectangular strain shadow where few faults develop occurs symmetrically in the hanging wall and footwall of fault F1 in the lower brittle layer (MLB), and has a length of ~20 km and a width of ~10 km (Fig. 2c). Thirdly, faults are more linear at depth (Fig. 2c), whereas they show more irregular and zig-zag geometry above the layer containing the pre-existing weakness (Fig. 2a–b).

New faults generally dip at 60°, and have two dominant strikes, NW-SE, parallel to the pre-existing plane of weakness, and N-S, i.e. perpendicular to the extension direction (Fig. 2). The longest fault, F1, consists of two segments in the lower brittle layer (Fig. 2b–c). One segment is F1a, representing the reactivated pre-existing weakness which strikes NW-SE and is ~25 km long. The other segment, F1b, strikes N-S, perpendicular to the extension direction and is ~4 km long. Each 'saw-tooth' fringe along the upper tip of F1a is ~3 km long in the upper brittle layer. The majority of faults away from the reactivated pre-existing weakness are generally extension-perpendicular, dipping E and W, 5–15 km long and with a curvilinear geometry in the plan view (Fig. 2).

A few faults, close to fault F1 (< 5 km away), strike near perpendicular to the pre-existing weakness. For example, fault F2, terminating against F1a on the middle horizon of the lower brittle layer, is sub-perpendicular to F1a and changes to be perpendicular to the extension direction approximately 5 km away from F1a (Fig. 2c). In addition, faults F3 and F4 show a similar strike direction sub-perpendicular to F1a at the bottom of the upper brittle layer (Fig. 2).

4. Fault evolution

The evolution of the two- and three-dimensional fault geometry is described with respect to four consecutive stages of extension in Fig. 3, 0–10% and three subsequent stages at increments of 5% extension (10–15%, 15–20% and 20–25%). Fault length, shape and throw distribution are described and compared between these stages (Fig. 4), in order to illustrate the evolution of the pre-existing weakness and adjacent new faults.

4.1. Reactivation of pre-existing structure and nucleation of new faults (0–10% extension)

Faults developing during the first stage of the extension history have two strike directions: NW-SE and N-S, i.e. extension-perpendicular (Fig. 3a–c). The NW-SE-striking segment, F1a, is directly related to the reactivation of the pre-existing weakness and has a similar length (~20 km) and rectangular shape (Fig. 4a). The upper tip line of F1a has an irregular geometry resembling seven 'teeth', some extending above the top of the pre-existing weakness (Fig. 4a). The lower tip line is more horizontal and linear, located about 2 km above the bottom of the pre-existing weakness (Fig. 4a). Throw on F1a is ≤ 20 m, without an apparent throw maximum (Fig. 4a). The D_{max}/L ratio of the segment is ~1/1000 (Fig. 4f).

Extension-perpendicular faults during the initial 10% of extension are much shorter that F1a, ranging from 1 to 5 km, and their lengths decrease with depth (Fig. 3a–c). For example, the extension-perpendicular segment F1b is 2 km long and has an approximately elliptical shape and is mainly located in the lower brittle layer (Fig. 4a). F1b has a throw maximum in 20 m, i.e. similar to F1a, and a D_{max}/L ratio of ~1/100 (Fig. 4a and f).

Approximately 80% of the pre-existing weakness reactivates during the first 10% extension. More specifically, F1a quickly reaches a length equivalent to the pre-existing weakness, but with a maximum throw similar to the extension-perpendicular faults that are much shorter. Accordingly, F1a has a low D_{max}/L ratio, and is highly under-displaced in comparison to extension-perpendicular faults in the model (Fig. 4f).

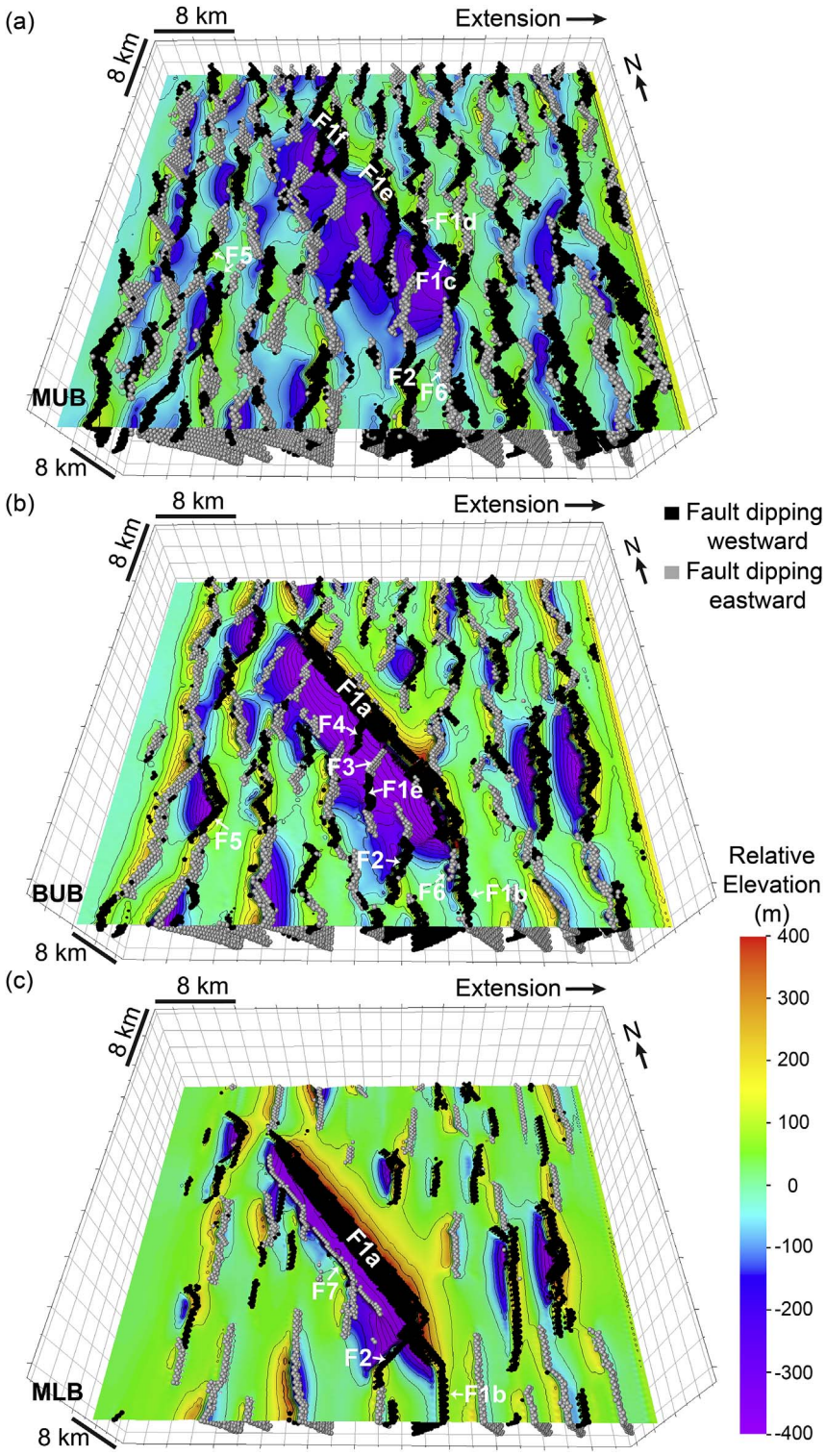

Fig. 2. Three horizons and faults offsetting the horizon at the final stage of extension (after 25% extension), viewed from the south. (a) Middle of the upper brittle layer (MUB). (b) Bottom of the upper brittle layer (BUB). (c) Middle of the lower brittle layer (MLB). The color bar from purple to red is for the relative elevation of the horizons. The light and dark grey elements represent the fault planes. See Fig. 1d for the depth of each horizon. (For interpretation of the references to colour in this figure legend, the reader is referred to the web version of this article.)

The lack of an apparent throw maximum on the major segment of F1a suggests that the segment reactivated approximately at the same time. The 'saw-tooth' upper tip line of F1a suggests limited upward growth of the pre-existing weakness.

4.2. Radial propagation and interaction between the reactivated structure and new faults (10%–15% extension)

Between 10 and 15% extension, the lateral tips of F1a propagate out from the pre-existing weakness within the lower brittle layer and have a mainly N-S strike, forming a twisted fringe (Fig. 3e–f). Each fringe grows to ~2 km long, making the whole segment F1a ~24 km long. The 'saw-tooth' upper tip line of F1a continues to propagate upwards and some of the teeth link together (Fig. 4b). In contrast, the lower tip of F1a does not change much (Fig. 4b). Segment F1a develops a long and flat elliptical center with a throw maximum of ~200 m and its D_{max}/L ratio increases significantly to ~1/100 (Fig. 4b). In response to the growth of F1a, a long and narrow subsidence center, ~20 km long and ~3 km wide, develops in the hanging wall of F1a (Fig. 3f). Comparison of T-z profiles along the length of F1a shows that fault throw

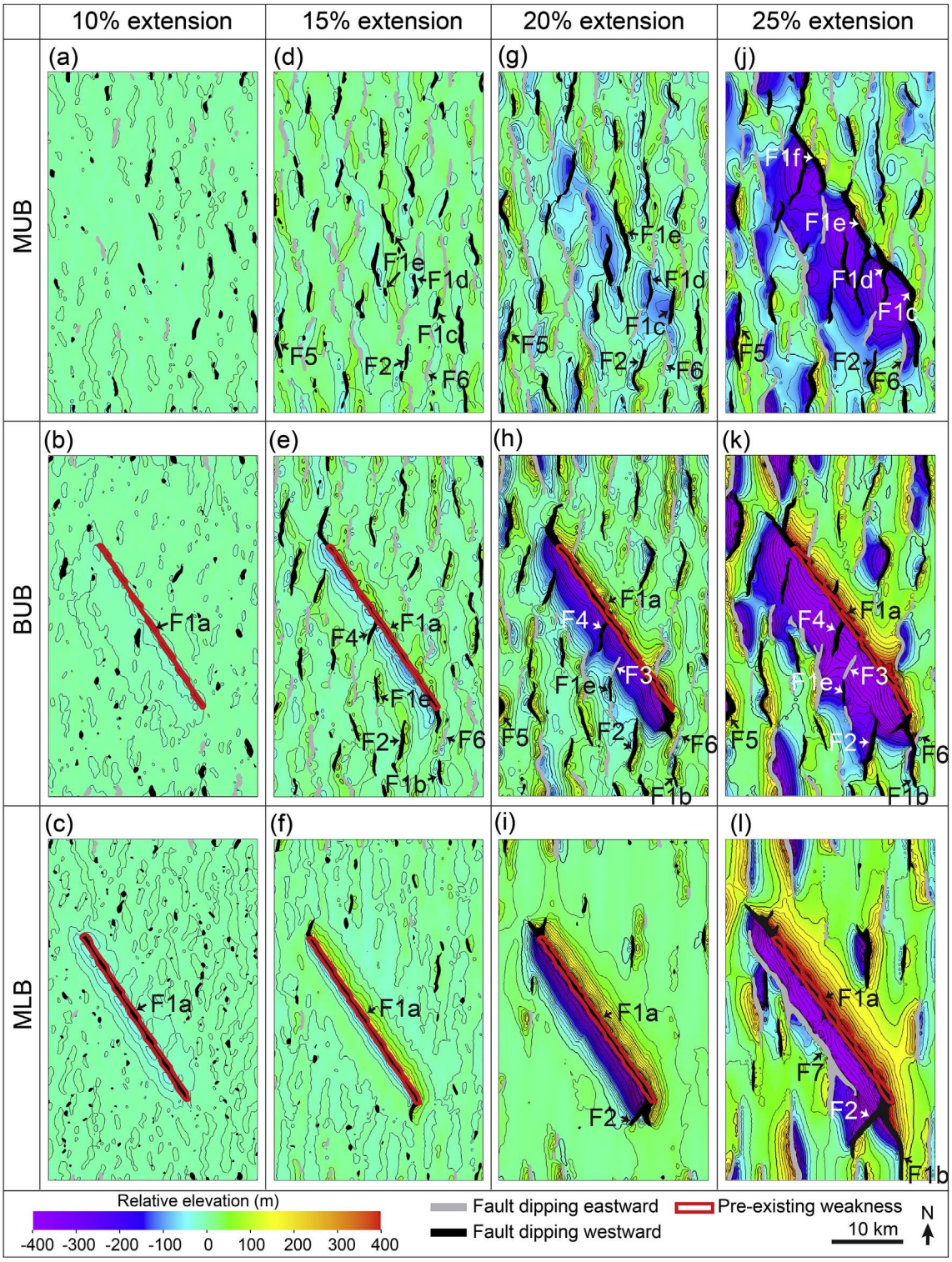

Fig. 3. Surface maps with line drawing of fault polygon at three horizons in both the upper and lower brittle layers during four stages of extension. MUB – middle of the upper brittle layer. BUB – bottom of the upper brittle layer. MLB – middle of the lower brittle layer.

changes rapidly near the tips, and then flattens out to form a plateau-type throw profile with a throw maximum at 6–8 km by 15% extension (Fig. 4e).

By 15% extension, extension-perpendicular faults have throws that do not exceed 100 m and are between 2 and 5 km long (Fig. 3d–f). For example, fault F1b achieves a length of ~3 km, a throw maximum of 100 m and a D_{max}/L ratio of ~1/30 during this interval of extension (Figs. 3e and 4b, f). F1b also has a plateau-type T-z profile, with the throw maximum at a depth of ~6 km (Fig. 4e). Compared to the initial stage of extension (0–10%), the plane of segment F1b propagates radially (Fig. 4b).

Not all newly formed faults strike perpendicular to the extension direction. For example, F1e in the upper brittle layer is a small, ~4 km long fault that strikes parallel to and is located above F1a (Fig. 3d). Another example is fault F4 that is ~3 km long and develops at a high angle to F1a at the bottom of the upper brittle layer, forming the

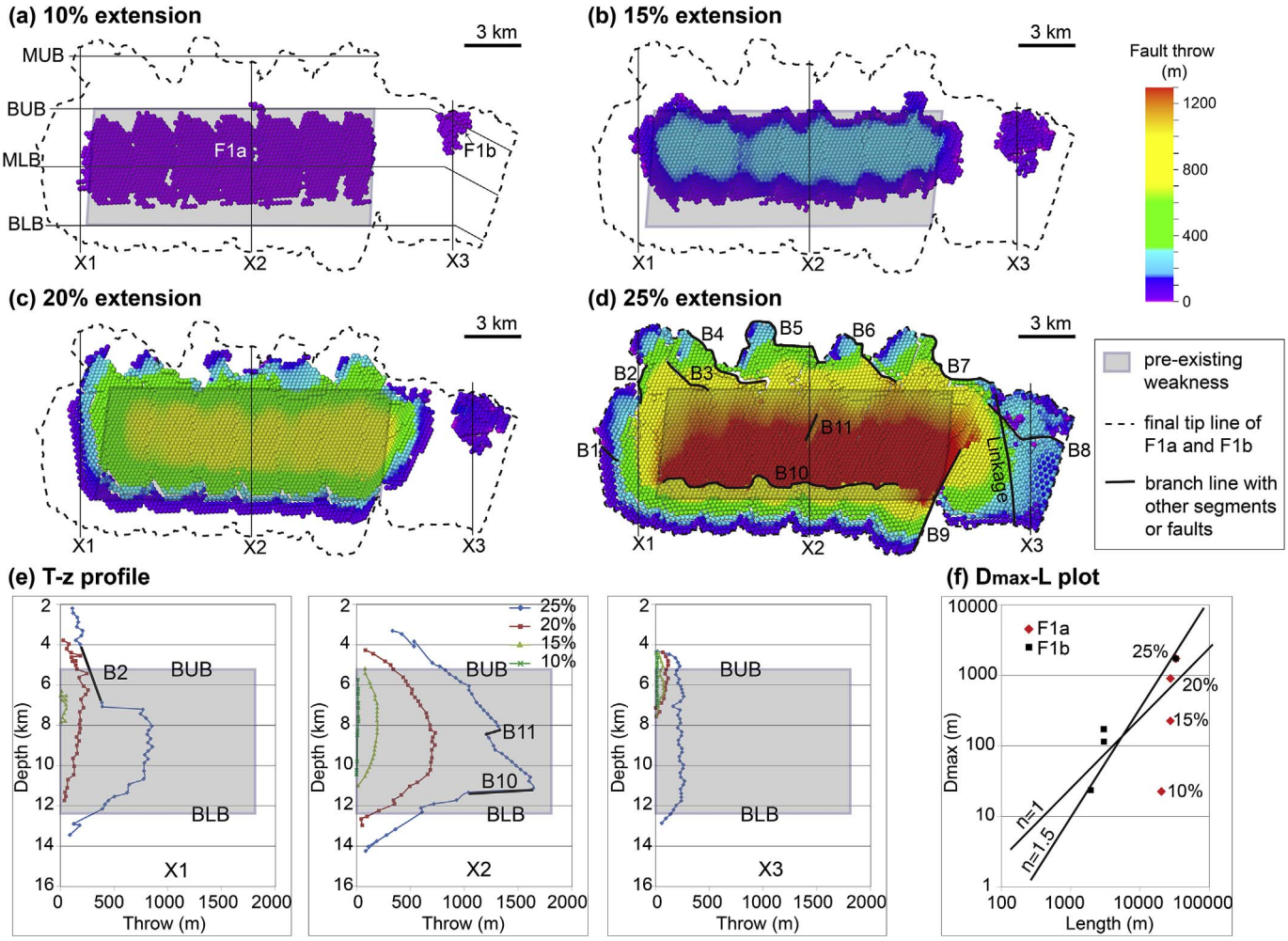

Fig. 4. Strike projections of F1 viewing from the southwest of the model, with T-z profile and D_{max}-L plots at four time stages during the extension. (a)–(d) Strike projection of F1. Branch lines (B1-B11) represent the intersections between F1 and surrounding faults. Vertical lines (X1-X3) indicate the location of T-z profile in (e). (e) T-z profile of three sections perpendicular to F1. (f) Plots of displacement maximum (D_{max}) against fault length (L). n in the plot corresponds to the constant in the scalar relationship $D = cL^n$ (e.g. Walsh and Watterson, 1998; Cowie and Scholz, 1992; Gillespie et al., 1992; Dawers et al., 1993; Schlische et al., 1996). MUB – middle of the upper brittle layer. BUB – bottom of the upper brittle layer. MLB – middle of the lower brittle layer. BLB – bottom of the lower brittle layer.

abutting interaction (Fig. 3e). In the lower brittle layer, however, a ~10 km wide and ~20 km long strain shadow zone, where fault density is very low compared to surrounding areas, develops along the entire length of F1a (Fig. 3f). These examples suggest that the activity on F1a influences the fault pattern developed in its immediate environment. In the lower brittle layer, deformation concentrates on the pre-existing weakness itself, hindering the formation of new faults in its proximity. In the upper brittle layer, the pre-existing structure influences the strike of adjacent faults, and favors the development of faults parallel or sub-perpendicular to it.

4.3. Radial propagation and interaction between the reactivated structure and new faults (15%–20% extension)

During 15–20% extension, the tips of F1a continue to propagate laterally, with an increase in length from ~24 km to ~26 km (Fig. 4c). The 'saw-tooth' fringe along the upper tip of F1a continues to propagate upwards, reaching to a level that is ~2 km above the lower brittle layer, and the lower part of the 'saw-tooth' fringes link and become continuous (Fig. 4c). The lower tip of F1a propagates beyond the base of the pre-existing weakness and into the lower crust (Fig. 4c). Throw maximum on F1a increases rapidly from ~200 m to ~800 m, and the D_{max}/L ratio approaches 1/30 (Fig. 4f). The T-z profile of F1a changes from a plateau to an asymmetric type, with the throw maximum deepening (X2 in Fig. 4e). These observations show that F1a continues propagating radially, with the 'saw-tooth' fringe heightening into the upper brittle layer.

Other faults also lengthen and heighten, reaching an average length of 6–8 km in the upper brittle layer (Fig. 3g–i). Throw maxima on extension-perpendicular faults are normally less than 200 m (Fig. 4g–i). The length of F1b increases from ~3 km to ~3.5 km (Fig. 4c), and the throw maximum increases from ~100 m to ~150 m, giving a D_{max}/L ratio of ~1/20. In general, the rate of increase in fault throw on extension-perpendicular faults is much lower than F1a.

In the lower brittle layer, the strain shadow zone in the hanging wall and footwall of F1a maintains a constant width and length (Fig. 3f). In addition, a new fault segment (F2), ~3 km long, develops perpendicular to fault F1a at the northeast boundary of the shadow zone, forming an abutting fault similar to F4 (Fig. 3i). Hence, this strain interval is also characterized by radial propagation and interaction between the pre-existing structure and adjacent new faults.

4.4. Linkage between the reactivated structure and adjacent new faults (20%–25% extension)

Between 20 and 25% extension, the upper tip of F1a continues upward propagation, reaching a higher level that is ~4 km above the lower brittle layer (Fig. 4d). Linkage of the 'saw-tooth' fringe of F1a

leads to a further reduction in the number of teeth (Fig. 4d). The lateral tips of F1a also continue to propagate, and the southeast tip of F1a links laterally with F1b (thick dashed line in Fig. 4d), forming a level-limited continuous non-planar fault (Fig. 3k–l). As a result of this linkage, there is a sudden increase in the length of F1 (F1a + F1b) from ~26 km to ~33 km. Throw maximum on F1a increases from ~800 m to ~1500 m, and the D_{max}/L ratio increases from ~1/30 to ~1/20, giving a near vertical trajectory from 10% to 25% extension in D_{max}-L space (Fig. 4d and f). The T-z profile for F1a has an asymmetric bell shape, with the few sites of significant change in throw related to intersections with surrounding faults (e.g. B10 in Fig. 4d and e).

As a result of the linkage between F1a and F1b, F1b loses its centrally located throw maximum owing to the significantly bigger fault throw on F1a (Fig. 4d). The trajectory of D_{max}/L of F1b from 10% to 25% extension shows a gentle gradient between n = 1 and n = 1.5, in contrast to the near vertical gradient of F1a (Fig. 4f). F1b maintains a plateau-type T-z profile, and extends downward from ~8 km to ~13 km (X3 in Fig. 4e). Hence, the linkage between F1a and F1b modifies the displacement distribution on F1b, masking the initial segmentation of F1a and F1b in the final displacement distribution.

Fault F1e links vertically with the underlying F1a at the branch line B5, and it also links laterally with some extension-perpendicular fault segments, to create a zig-zag or twisted fault geometry (Figs. 2a, 3j and 5b). The abutting fault, F2, grows to ~7 km long in the lower brittle layer and varies in strike from perpendicular to F1a to perpendicular to the extension direction at a distance of ~5 km away from the segment F1a (Fig. 3l). F7, a new fault striking parallel and dipping opposite to F1a, forms in the hanging wall of F1a, located ~4 km away from F1a on the middle horizon of the lower brittle layer (Figs. 3l and 5c). The development of fault segments F1e, F2 and F7 that are parallel or perpendicular to F1a suggests a control exerted by F1a on the orientation of adjacent faults.

5. Fault interaction styles

Four styles of fault interactions develop around the pre-existing weakness: (i) isolated, (ii) abutting, (iii) twisting, and (iv) conjugate faults (Figs. 2 and 5). Key examples of each interaction style are described, focusing on their relationship with the pre-existing weakness (F1a) and the evolution of fault interactions with increasing strain.

5.1. Isolated faults

F5 is representative of extension-perpendicular faults that are isolated and have no interaction with F1a (Fig. 2). Between 0 and 10% extension, several W-dipping segments (1–2 km long) of F5 nucleate and begin to grow; two segments nucleate in the upper part of the upper brittle layer, whereas four occur in the lower part of upper brittle layer (Fig. 6a). As extension increases to 15%, these segments propagate radially, increasing in length to 2–4 km (Fig. 6b). Between 15 and 20% extension, the lower four segments link together, generating a continuous segment that is ~10 km long, and has a throw maximum (~200 m) in the center (Fig. 6c). In addition, the upper two segments link and then connect to the lower four segments, giving rise to a single fault. However, a zone of throw deficit remains in the middle of fault F5, without linkage between the former segments. Between 20 and 25% extension, F5 keeps propagating radially, with its lower tip penetrating deeper into the lower brittle layer (Fig. 6d). By 25% extension, F5 has an elliptical form and a central throw maximum of ~600 m (Fig. 6d). The accumulation of strain and subsequent linkage between segments largely masks the initial segmentation of the final fault plane (Finch and Gawthorpe, 2017). The modeling result suggests that isolated faults away from the influence of the pre-existing weakness form via radial propagation and linkage of fault segments.

5.2. Abutting faults

A typical example of an abutting interaction is found where F2 abuts against F1a (Fig. 5a). Between 0 and 10% extension, four extension-perpendicular segments of F2 form away from F1a, mainly in the upper brittle layer in the hanging wall of F1a; one segment is larger than the other three (Fig. 7a). Between 10 and 15% extension, the four segments link vertically. Throw maximum (~100 m) is found in the upper part of the fault where the initially largest segment occurs (Fig. 7b). Between 15 and 20% extension, F2 accumulates throw and a new segment nucleates on the lower part of F1a and propagates orthogonally in the hanging wall of F1a. The throw maximum (~100 m) of this new segment is at the branch line with F1a (B9 in Fig. 7c). By 25% extension, the new segment links with F2 obliquely (Fig. 7d). Even though the new segment of F2 nucleating on F1a develops later than the other four segments, its final throw maximum (~800 m) is larger than that of the other four segments.

5.3. Twisting faults

A representative example of a twisting fault is F1e that develops in the upper brittle layer above F1a (Fig. 5b). Between 0 and 10% extension, three preliminary segments of F1e nucleate in the upper brittle layer above F1a, with a throw maximum of ~20 m. One segment is parallel to and just above F1a; the other two are extension-perpendicular and located in the hanging wall of F1a (Fig. 8a). Between 10 and 15% extension, the three segments propagate radially and the two extension-perpendicular segments link vertically, with an increase in throw maximum from ~20 m to ~100 m (Fig. 8b). By 20% extension, the segment just above F1a starts to soft-link laterally with the extension-perpendicular segments, accompanied by vertical soft-linkage with the upper tip of F1a (Fig. 8c). The strike of the northern tip of F1e swings to be extension-perpendicular as it propagates laterally away from F1a (Fig. 8c). Between 20 and 25% extension, the segments of F1e link laterally, and become hard-linked with F1a (Fig. 8d). The growth and linkage of the segments of F1e leads to a twisting geometry, with the segment parallel to the underlying F1a in the middle and two extension-perpendicular segments at its extremities (Fig. 8d). The branch line marking the linkage between F1a and F1e is the place of the final throw maximum (~400 m) on F1e, suggesting that the pre-existing structure enhances the displacement of the segment that directly links to it.

5.4. Conjugate faults

Two types of conjugate faults develop depending on the timing of their initiation. Type 1 involves two faults that initiate at the same time, while Type 2 refers to the case where one fault initiates earlier than the other.

F6 and F1b represent Type 1 conjugate faults. F6 evolves as four N-S-striking, E-dipping segments linking up and interacting with the N-S-striking, W-dipping F1b (Fig. 9a). As both F1b and F6 propagate between 10 and 15% extension, the southern tip of F6 interacts with the northern tip of F1b. In addition, a new E-dipping segment of F6 nucleates to the south of F1b (Fig. 9b). By 20% extension, F1b is laterally retarded by the segments of F6, which in turn are retarded by F1b (Fig. 9c). However, the northern tip of F1b continues to propagate laterally below F6 (Fig. 9c). Between 20 and 25% extension, F1b links laterally with F1a below F6 (Fig. 9d). Similarly, the segments of F6 link together below F1b. At the branch line between the conjugate faults, the fault offset is minimal (< 100 m).

The interaction of F7 with F1a exemplifies the formation of Type 2 conjugate faults. F1a is active from 10% extension (Fig. 10a), whereas F7 forms very late, between 20 and 25% extension (Fig. 10d). Fault F7 nucleates along the lower part of F1a, with its upper tip vertically linking with five extension-perpendicular faults in the lower brittle

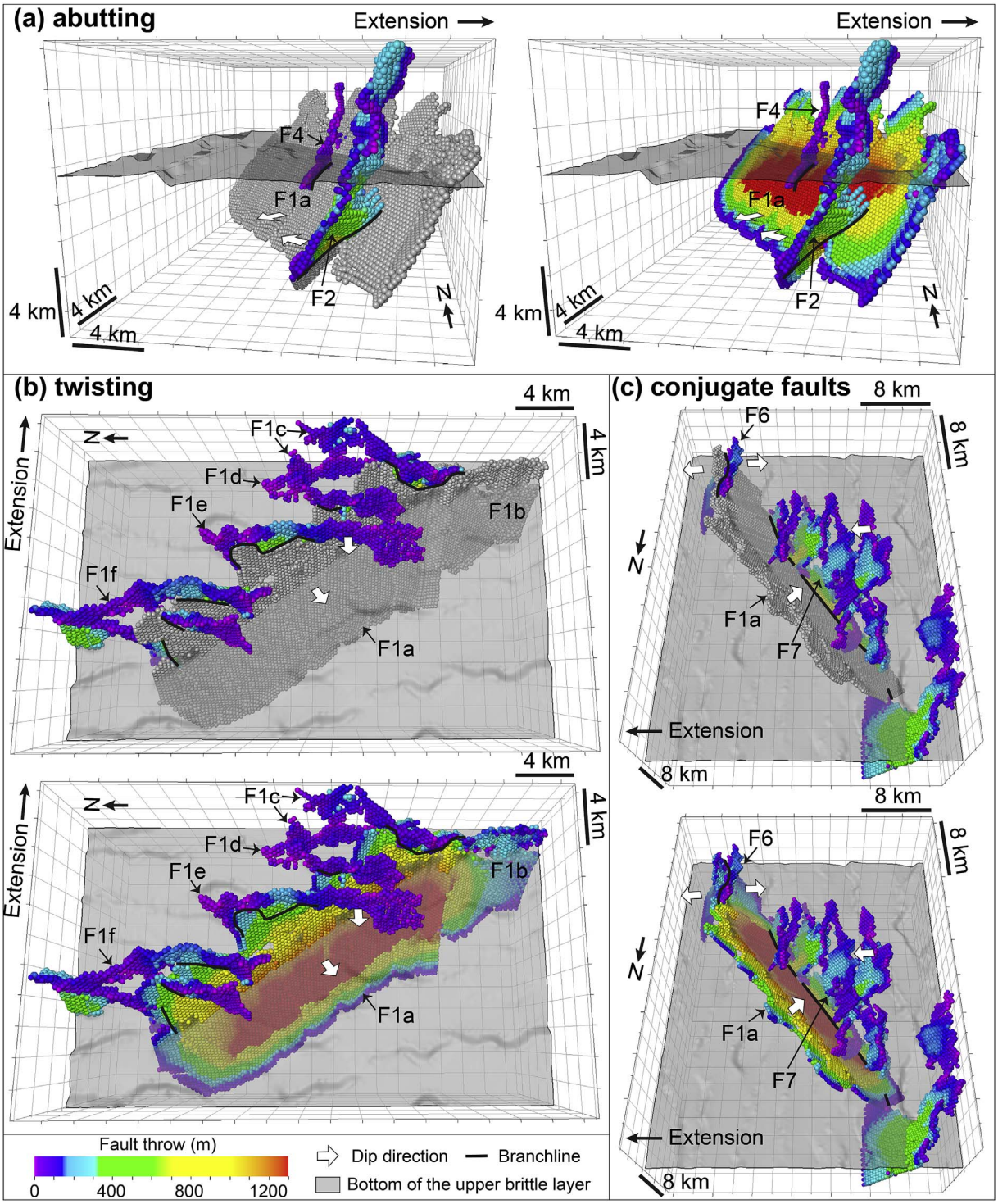

Fig. 5. 3D geometry of fault interaction styles observed in the final stage of extension. (a) Abutting, (b) Twisting, and (c) Conjugate faults. For each interaction style, fault pattern is shown with and without the throw projected on the fault F1a, in order to differentiate the extension-perpendicular fault from the reactivated pre-existing fault. Fault throw is coloured from purple (0 m) to red (1.2 km). Black lines represent branch lines at intersections between fault pairs. Faults are named for discussion in the text. The grey transparent plane represents the bottom of the upper brittle layer (BUB). (For interpretation of the references to colour in this figure legend, the reader is referred to the web version of this article.)

layer (A1-A5 in Fig. 10d). The five extension-perpendicular faults initiate very early in the upper brittle layer, between 0 and 10% extension (Fig. 10a). The final throw maximum on F7 is 800 m, occurring at the branch line with F1a (B10 in Fig. 10d). In contrast, the extension-perpendicular faults have a final throw maximum of 400 m (Fig. 10d). Even though initiating much later than the five extension-perpendicular faults, F7 accumulates greater throw than the extension-perpendicular faults.

6. Discussion

The evolution of a normal fault network affected by a pre-existing planar weakness oblique to the extension direction is examined, and can be summarized in three stages. During the first stage, reactivation of the pre-existing weakness and nucleation of new faults occurs, generating a reactivated structure that is highly under-displaced and propagates upwards via a 'saw-tooth' fringe (Fig. 11a). During the second

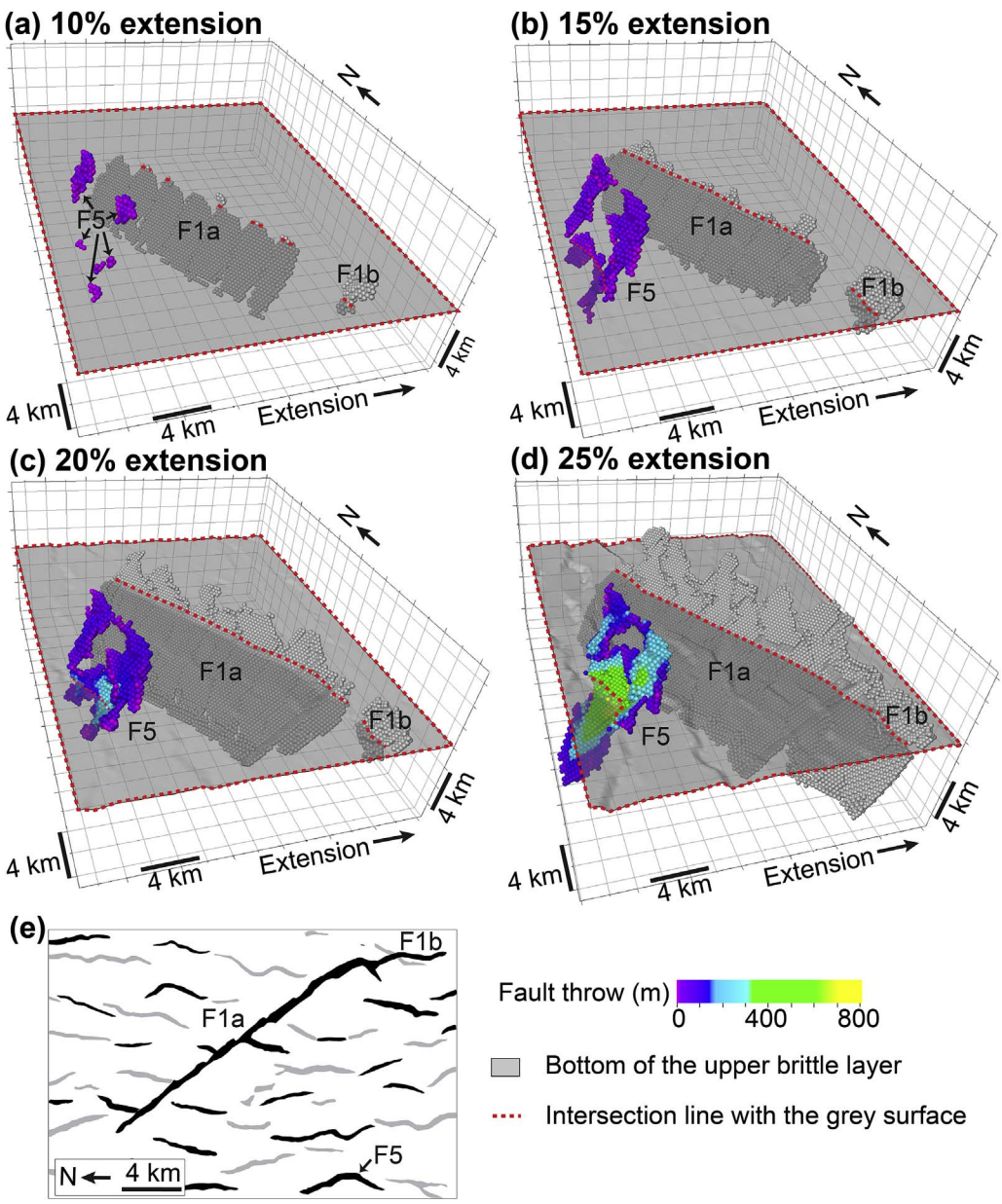

Fig. 6. 3D fault geometry for the isolated fault (F5) from the reactivated pre-existing weakness, F1a, during four stages of extension. (a) 10% extension. (b) 15% extension. (c) 20% extension. (d) 25% extension. (e) Map of fault trace at the bottom of the upper brittle layer at 25% extension. Grey faults are E-dipping whereas black faults are W-dipping. Grey transparent plane represents the bottom of the upper brittle layer (BUB).

stage, the reactivated structure and new faults propagate radially and interact, with a strain shadow zone in the proximity of the reactivated structure, where fault density decreases and the strike of new faults is perpendicular or highly oblique to the reactivated structure (Fig. 11b). Fault interactions, such as abutting, twisting and conjugate faults, start to occur between the reactivated structure and adjacent new faults (Fig. 11b). During the third and final stage, the reactivated structure links with adjacent faults, creating non-planar fault geometries (Fig. 11c).

6.1. Reactivation and growth of pre-existing structures

Walsh et al. (2002) proposed a 'near-constant' fault growth model where normal faults rapidly obtain their near-final length, followed by a long period of displacement accrual, which is directly applicable to reactivated fault systems. Also, Childs et al. (1995, 1996) suggested that individual fault segments initiate and grow as kinematically related components of a fault array, becoming hard-linked to a single fault over time in a coherent fault model. Our modeling results show many similarities to the fault growth models of Childs et al. (1995, 1996) and Walsh et al. (2002). The first similarity is that the pre-existing weakness is reactivated and ruptured along its entire length very quickly, within the first 10% of extension in our model, which is followed by a long period of displacement accumulation without significant lateral propagation. The D_{max}/L ratios for the reactivated weakness (F1a) and new faults are plotted on Fig. 12 to compare with natural examples of normal faults (Kim and Sanderson, 2005). Fig. 12 shows that the D_{max}/L ratio of the reactivated structure (F1a) at 10% extension plots well below the best fit line obtained from natural examples of normal faults (the dashed line in Fig. 12). As strain increases and displacement accumulates on the reactivated pre-existing weakness, it develops a D_{max}/L ratio similar to natural faults. In D_{max}-L space the pre-existing weakness follows a near vertical trajectory, whereas the newly formed extension-perpendicular faults in the model plot close to the best fit D_{max}/L line during their entire growth history (Fig. 12). The second similarity is that the vertical propagation of the reactivated structure resembles the coherent model of fault growth (Childs et al., 1995, 1996; Walsh et al., 2002, 2003; Baudon and Cartwright, 2008; Giba et al., 2012). The irregular upper tip line of the reactivated structure shows that it propagates into the overlying rocks by the formation of 'saw-

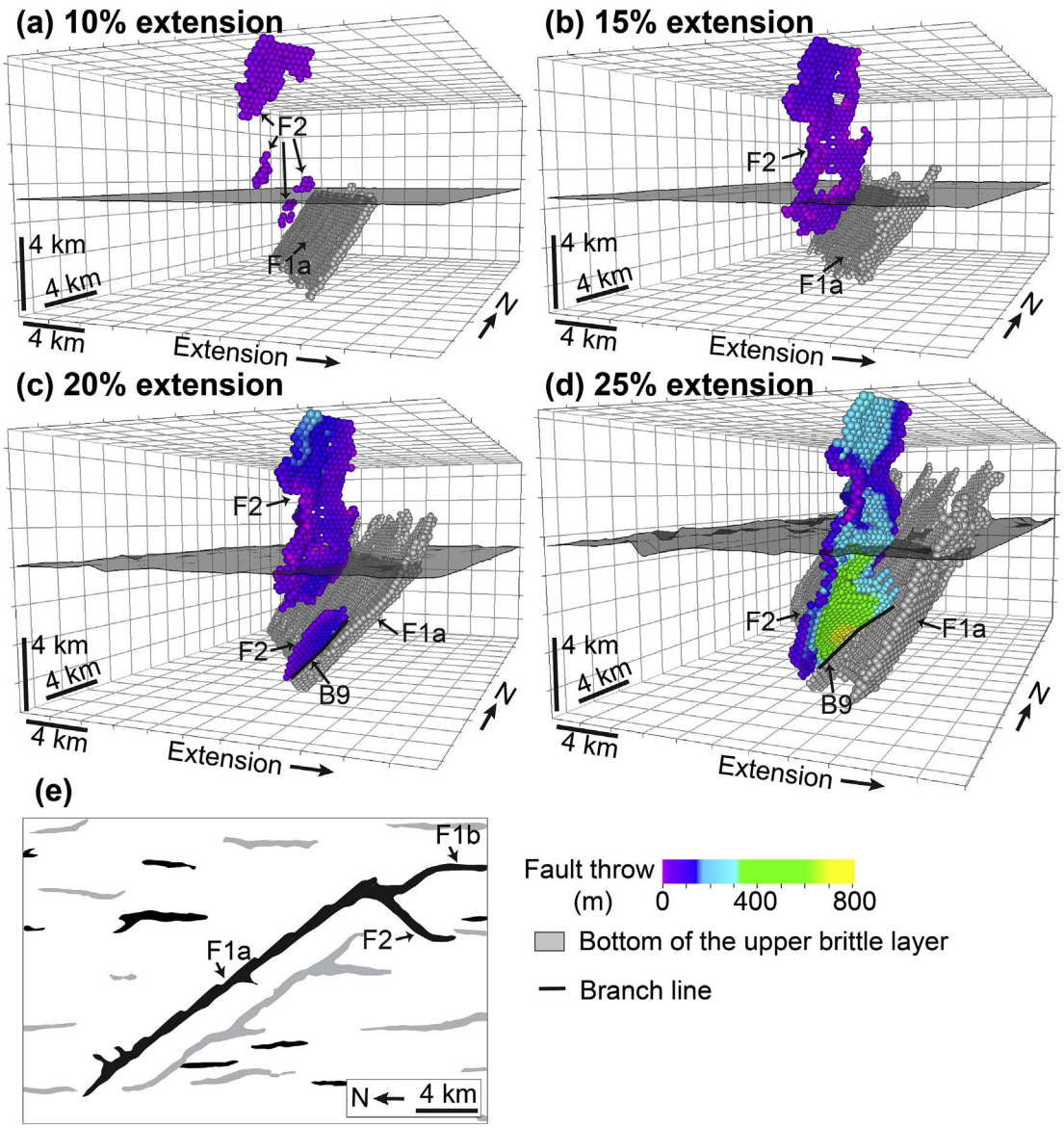

Fig. 7. 3D fault geometry for the fault (F2) abutting against the reactivated pre-existing weakness, F1a, during four stages of extension. (a) 10% extension. (b) 15% extension. (c) 20% extension. (d) 25% extension. (e) Map of fault trace in the middle of the lower brittle layer (MLB). Grey faults are E-dipping whereas black faults are W-dipping. Grey transparent plane represents the bottom of the upper brittle layer (BUB).

tooth' fringes. These 'saw-tooth' fringes coherently propagate, interact and hard-link over time as strain accumulates, behaving like the kinematically related segments of a fault array in the coherent model of Childs et al. (1995, 1996). Hence, the growth of 'saw-tooth' fringes or kinematically related fault segments should be the prevalent growth model for a fault related to the reactivation of a pre-existing structure in nature (see also Fossen and Rotevatn, 2016).

In our model, the growth history of the pre-existing structure is characterized by synchronous nucleation of new fault segments and reactivation of the pre-existing structure separately in the upper and lower brittle layers, followed by radial propagation and final dip linkage as strain accumulates (Fig. 11). These observations suggest that strain is simultaneously accommodated on both the pre-existing weakness in the lower brittle layer and newly-formed fault segments in the upper brittle layer. It is obvious that strain localization on the pre-existing structure is more significant owing to its weaker bond strength and initial size (Walsh et al., 2001). However, strain is more distributed in the upper brittle layer as indicated by generally short, isolated and widely-spread newly-formed fault segments. Jackson and Rotevatn (2013) described a similar fault evolution for a salt-influenced normal fault zone in Suez Rift where supra-salt fault segments nucleated in the Pliocene strata during the early Pliocene, and propagated downwards and linked to a reactivated sub-salt fault system. Thus, they suggested that Pliocene extension was accommodated on both the sub- and supra-salt fault systems, which is consistent with our modeling results that newly-formed fault segments initially grow decoupled from the reactivated structure and link later in their growth history.

6.2. Impact of a pre-existing structure on adjacent fault network

From the modeling results, the impact of a pre-existing structure on the geometry and evolution of the adjacent fault network includes variations in the fault density, strike, dip and displacement, and also in providing a nucleation site for neighboring new faults.

Fault density is lower in the ~5 km strain shadow zone along the pre-existing structure in the lower brittle layer. In this zone, few faults develop as strain is largely accommodated on the weak pre-existing structure than in the surrounding rock. Such an effect indicates that the reactivated structure retards the growth of new faults in its proximity, related to the zone of stress reduction that occurs around faults (e.g.

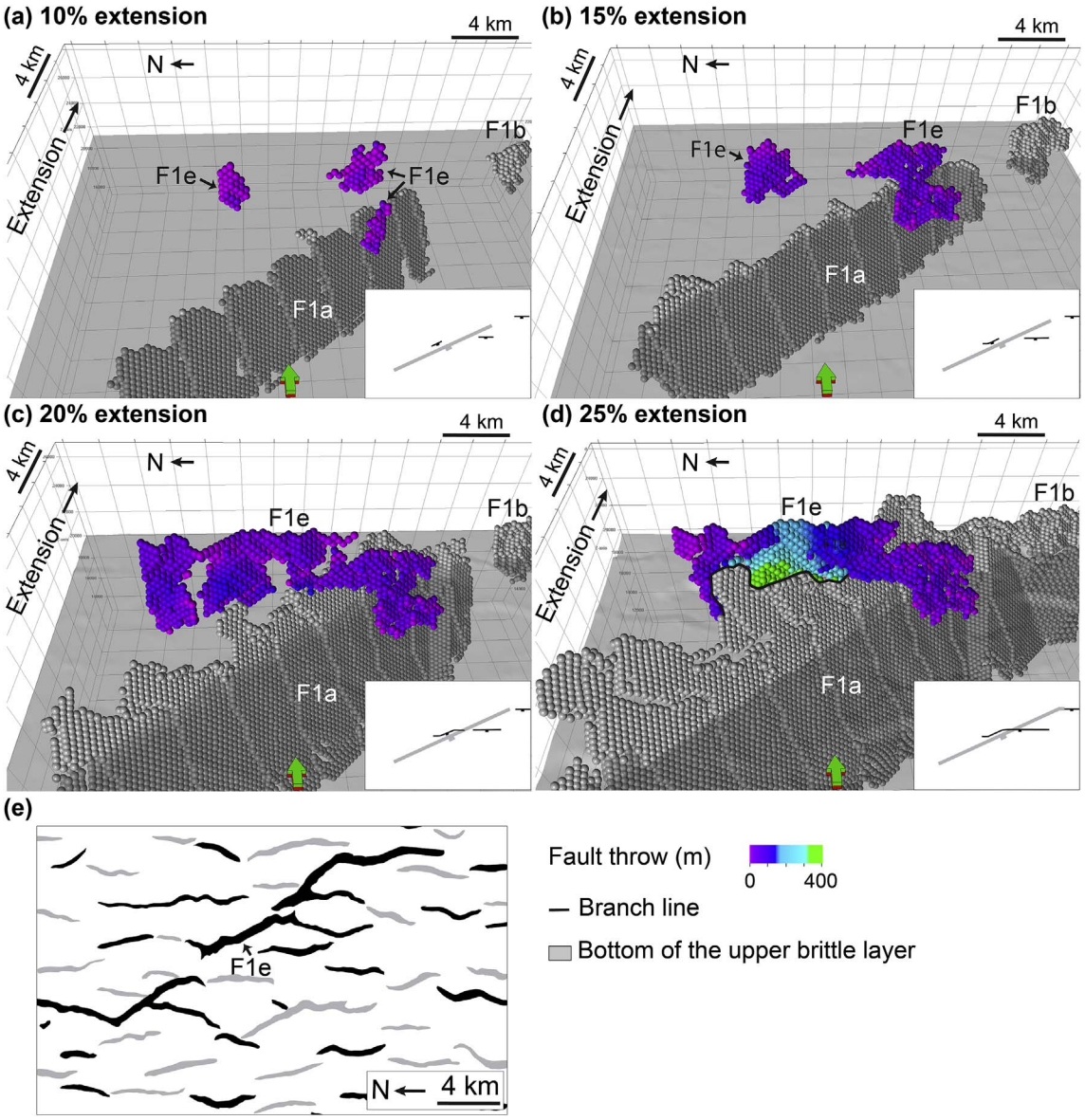

Fig. 8. 3D fault geometry for the twisting fault (F1e) influenced by the underlying reactivated pre-existing weakness, F1a, during four stages of extension. (a) 10% extension. (b) 15% extension. (c) 20% extension. (d) 25% extension. (e) Map of fault trace in the middle of the upper brittle layer (MUB). Grey faults are E-dipping whereas black faults are W-dipping. The grey transparent plane represents the bottom of the upper brittle layer (BUB).

Willemse et al., 1996; Ackermann and Schlische, 1997; Gupta and Scholz, 2000; Cowie and Roberts, 2001; Soliva et al., 2006). Ackermann and Schlische (1997) found a critical stress-reduction shadow that prevented the nucleation of smaller faults in the vicinity of the master faults and suggested that the master faults formed earlier than the smaller faults. Furthermore, the effect of stress reduction was simulated by Gupta and Scholz (2000), who indicated that tip propagation can be retarded in the stress-reduction region of an overlapping fault. Our model results confirm that the reactivated structure quickly grows into a major fault and inhibits lateral propagation of adjacent new faults owing to the stress reduction in the strain shadow zone.

The reactivated structure influences the strike and dip of adjacent new faults. The modeling results show that some new faults nucleate at, and propagate away from the reactivated structure, striking sub-perpendicular and forming an abutting interaction. Fault F2 shows lateral and vertical variations in strike from sub-perpendicular to the reactivated structure to perpendicular to the extension direction, related to lateral and vertical linkage of initial segments of differing strike (Fig. 7). Henza et al. (2010, 2011) also reported that second-phase faults propagated outward from first-phase faults, with a strike ranging from perpendicular to the first-phase fault to perpendicular to the extension direction. Duffy et al. (2015) investigated the three-dimensional geometry of faults with abutting interactions in the northern North Sea. They found that a second-phase fault abutting against a first-phase fault has its displacement maximum at the branch line with the first-phase fault, and suggested that the first-phase fault served as a nucleation site for the second-phase fault. Our modeling results indicate that the displacement maximum of the abutting fault occurs at the branch line which is consistent with the nucleation site for the abutting fault (e.g., fault F2 in Fig. 7d). Therefore, reactivated pre-existing structures can provide the nucleation sites for new faults.

Furthermore, the reactivated structure influences the displacement of adjacent new faults, as indicated by F1e that has a central segment parallel to the reactivated structure and two extension-perpendicular segments at the edges (e.g. F1e in Fig. 8). The segment parallel to the reactivated structure is also the site of displacement maximum. These two, coincident, features of fault F1e indicate a significant influence of the reactivated structure on fault development. Such displacement

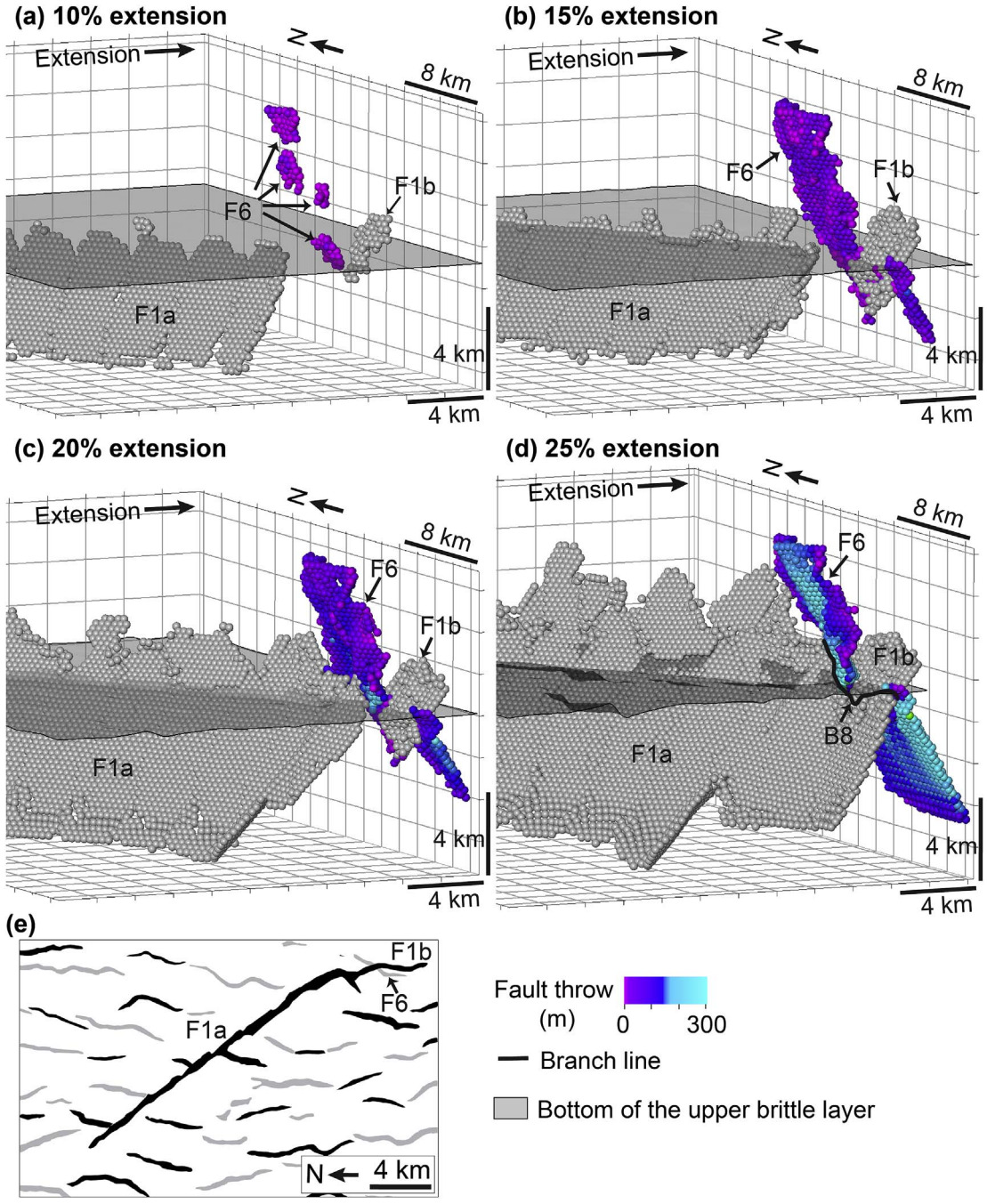

Fig. 9. 3D fault geometry for the Type 1 conjugate faults between F6 and the reactivated pre-existing weakness, F1a and F1b, during four stages of extension. (a) 10% extension. (b) 15% extension. (c) 20% extension. (d) 25% extension. (e) Map of fault trace in the bottom of the upper brittle layer (BUB). Grey faults are E-dipping whereas black faults are W-dipping. The grey transparent plane represents the bottom of the upper brittle layer (BUB).

enhancement on the fault segments immediately linking to the reactivated structure reflects strain localization on the reactivated pre-existing structure. The final displacement maximum positioned on the segment parallel to the reactivated structure may be mistaken for the nucleation point of the whole twisting fault F1e. However, our modeling results illustrate that the location of the final displacement maximum is related to linkage with the reactivated structure. This observation implies that analysis of final displacement distribution or D-L plots may not always reflect the nucleation site of a fault.

6.3. Implication for fault growth affected by a pre-existing structure

The advantage of a numerical modeling approach is that the nucleation, propagation and linkage of fault segments can be directly visualized, as opposed to being inferred from the final fault geometry and fault attributes such as D-L variations. Our study questions the interpretation of fault growth histories based on final D-L analysis as the location of displacement maximum may change as strain increases, especially when the displacement maximum is greatly affected by a reactivated structure. A reactivated structure can enhance the displacement of faults that link to it, changing the location of displacement maximum. The nucleation points of some initially isolated segments become masked as they do not preserve their initial, isolated displacement maximum following linkage. Thus, using the final displacement distribution to reconstruct the linkage history of a fault may not always lead to the correct interpretation and it may be impossible to

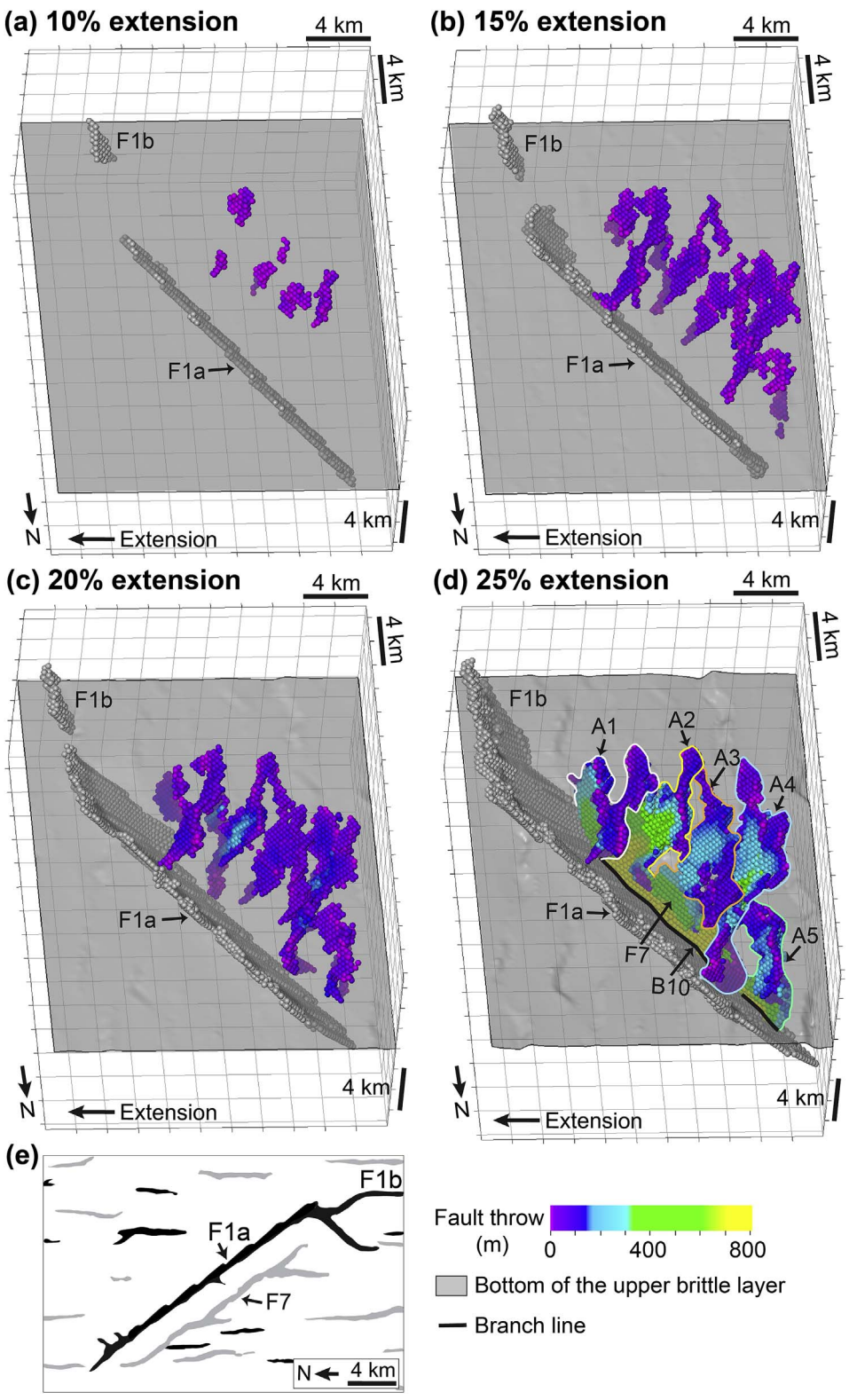

Fig. 10. 3D fault geometry for the Type 2 conjugate faults between F7 and the reactivated pre-existing weakness, F1a and F1b, during four stages of extension. (a) 10% extension. (b) 15% extension. (c) 20% extension. (d) 25% extension. A1-A5 are extension-perpendicular fault segments of fault F7. (f) Map of fault trace in the middle of the lower brittle layer (MLB). Grey faults are E-dipping whereas black faults are W-dipping. The grey transparent plane represents the bottom of the upper brittle layer (BUB).

extract the complete growth history from final fault displacement analysis alone.

Most multirift basins contain two or three differently oriented sets of faults such as the NW Shelf of Australia (Frankowicz and McClay, 2010), Gulf of Thailand (Morley et al., 2004, 2007), Gulf of Aden (Lepvrier et al., 2002; Bellahsen et al., 2006), and northern North Sea (Badley et al., 1988; Færseth, 1996; Færseth et al., 1997; Odinsen et al., 2000; Whipp et al., 2014; Duffy et al., 2015). In these natural examples, the fault network comprises both reactivated first-phase or pre-rift faults and new faults interpreted to have formed during secondary rift phase(s). For example, Whipp et al. (2014) mapped a conspicuous set of late Jurassic NW-SE-trending faults related to the second phase of North Sea rifting in part of the Horda Platform (northern North Sea rift, Fig. 13). These faults are locally twisted into a more N-S trend that corresponds to the trend of phase 1 rift structures (areas outlined by blue ellipses in Fig. 13). Several of these N-S structures were reactivated

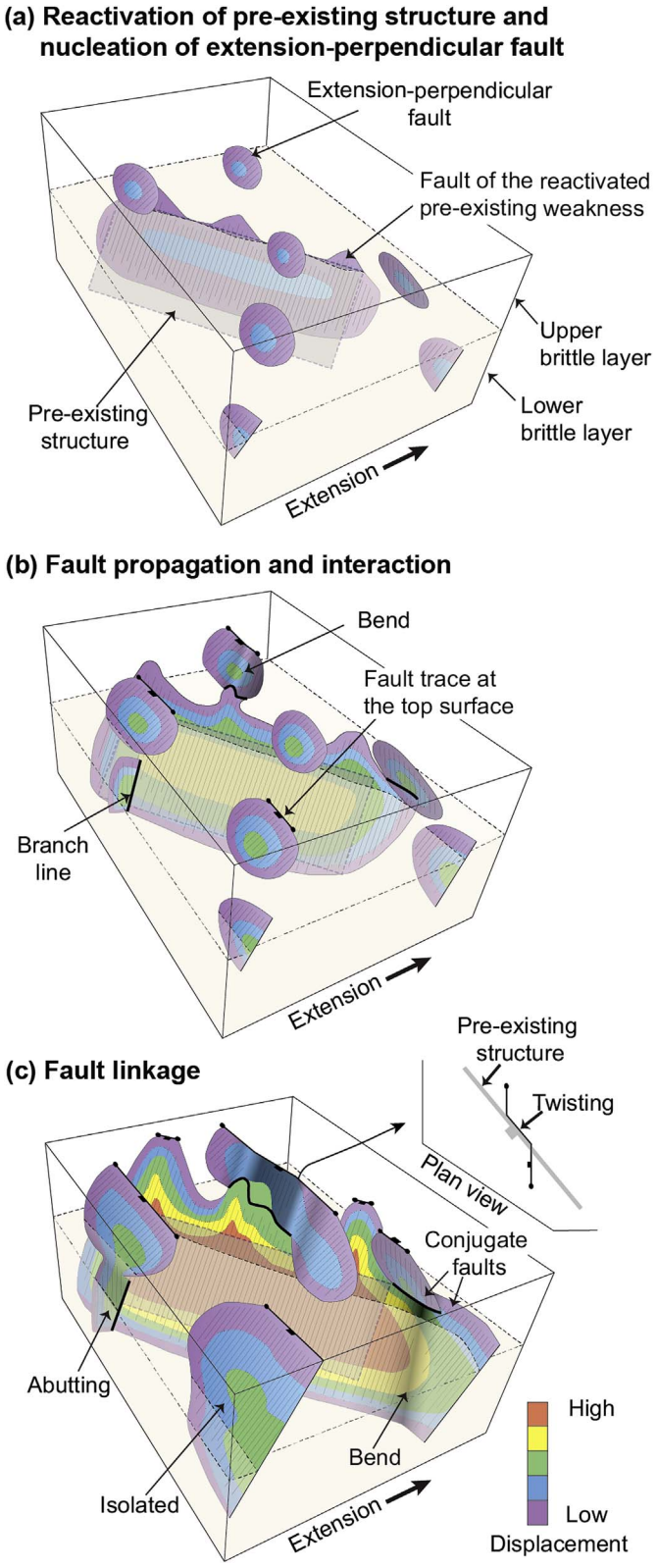

Fig. 11. Summary figure for fault evolution and fault interaction styles developing during an oblique extension relative to the pre-existing weakness. Black fault trace shows that the fault is surface breaking fault. Black line is the branch line at the intersection between fault pairs.

as major faults (grey lines in Fig. 13), but our focus here is on structures that did not propagate to the middle Jurassic level shown in Fig. 13. We suggest that the NW-SE-trending faults formed in response to NE-SW extension, and that their local rotation into N-S direction relates to influence by earlier underlying N-S faults. Furthermore, based on the results presented above, the zones of more N-S trending fault orientation may mark strain shadow zones related to these underlying structures.

In other cases, second-phase rift faults show a constant strike orientation, and are not affected by pre-existing underlying structures. The new faults would then be good indications of the extension direction associated with their formation, for example as argued by Deng et al. (2017) for NW-SE oriented second-phase rift faults in another part of the Horda Platform. In summary, to recognize the influence of the reactivation of a pre-existing structure on a fault network, fault strike, density, dip and displacement should all be considered. This work provides an example of the influence of a pre-existing planar weakness on the fault network, and is a precedent for understanding three-dimensional fault geometries and evolution affected by a pre-existing planar weakness.

7. Conclusions

Although we focus on one simple case of a weak plane dipping at 60° and striking 60° to the extension direction, the results of our modeling have general implications for normal fault networks developed in heterogeneous crust and rift basins subject to multiple phases of extension. The main findings are:

1. Reactivation of the pre-existing structure is rapid and widespread, resulting in a long and under-displaced fault, followed by a long period of displacement accumulation with limited increase in length. The reactivated structure accommodates more strain than extension-perpendicular faults, becoming the dominant fault in terms of size, displacement and influence on surrounding structures.
2. The reactivated pre-existing structure propagates upwards by 'saw-tooth' fringes or kinematically related fault segments similar to the coherent fault growth model.
3. The reactivated structure retards the growth of new faults in a strain shadow zone, a 5 km wide rectangular zone symmetrically distributing in the hanging wall and footwall of the reactivated structure.
4. The growth of the reactivated structure influences the orientations of new faults in its vicinity, with strikes sub-perpendicular to the reactivated structure. The reactivated structure also provides nucleation sites for new faults. In addition, down-dip slip of the pre-existing structure controls the development of new faults parallel to the pre-existing structure.
5. The reactivated structure also influences the displacement of new faults in its vicinity. New faults that link with a pre-existing structure have displacement enhancement at the branch line owing to the dominance of the pre-existing structure. Linkage of the reactivated structure and extension-perpendicular faults creates complex non-planar fault geometries.
6. Interpretation of fault propagation and linkage history based on final displacement distribution is not always possible, especially for new faults that interact and link with pre-existing structures. This is because displacement maxima in initially isolated segments may be masked after linkage with the dominant, higher displacement pre-existing structure.

In general, the influence of a pre-existing structure will add geometric complexity to the fault network during a rift phase, and hence lead to complications in estimating extension directions based on fault orientation alone. This work provides a theoretical example of a single pre-existing structure – in each natural example the orientations, geometries and distribution of such pre-existing structures must be taken into account, if possible, together with their mechanical strength.

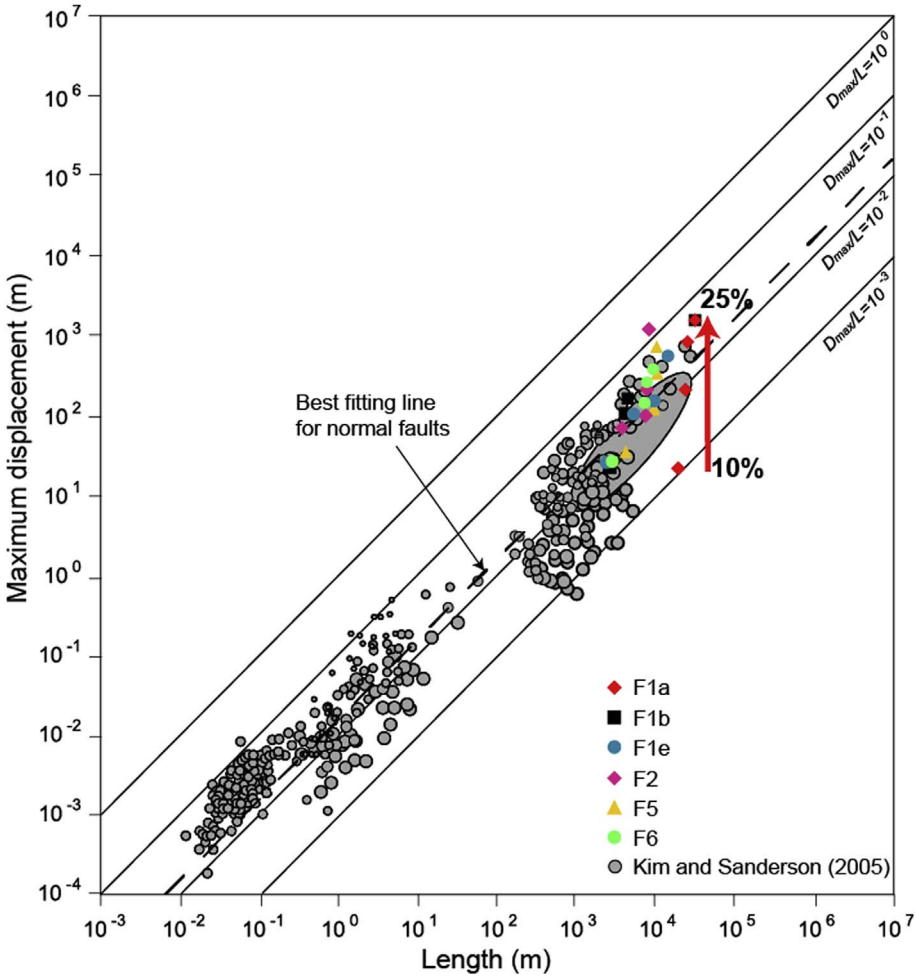

Fig. 12. Comparison between plots of maximum displacement against fault length of F1 during four stages of extension in the modeling result and natural examples from Kim and Sanderson (2005).

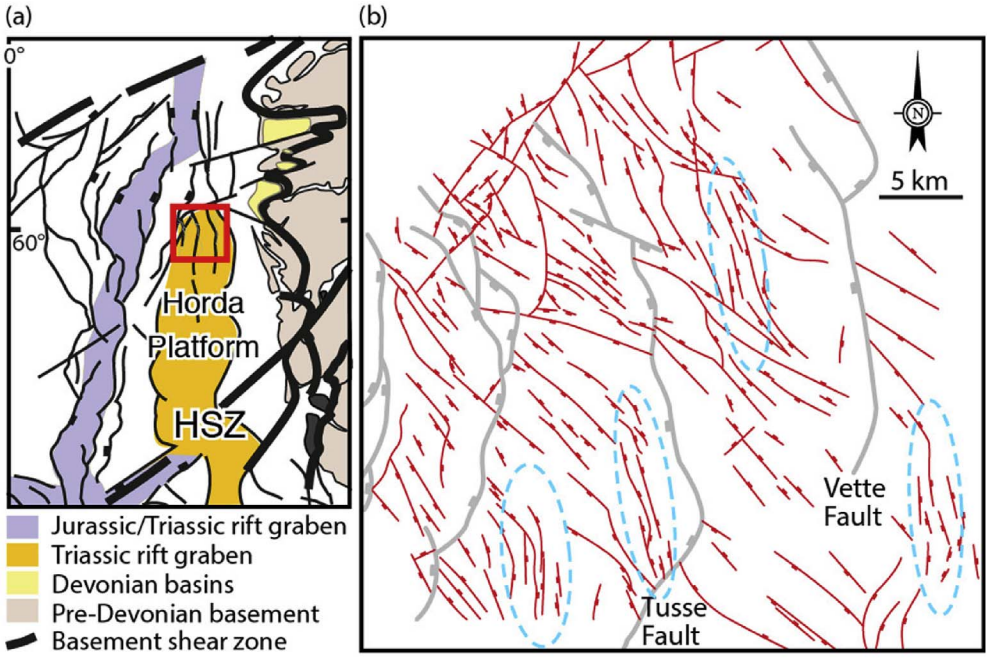

Fig. 13. a) Regional setting, and b) structural map of the Middle Jurassic top Brent Group in the northern Horda Platform, northern North Sea. Red lines represent faults formed during the second rift phase (late Jurassic), and ellipses outline regions where their general NW-SE trend is deflected. Based on Whipp et al. (2014). (For interpretation of the references to colour in this figure legend, the reader is referred to the web version of this article.)

Acknowledgement

This contribution forms part of the MultiRift Project funded by the Research Council of Norway's PETROMAKS program (Project number 215591) and Statoil to the University of Bergen and partners Imperial College, University of Manchester and University of Oslo. We thank members of the MultiRift project for discussion which helped focus the model presented in this paper. Schlumberger is thanked for academic Petrel licenses to the universities of Bergen and Manchester which is used to visualize the numerical modeling results. Tiago Alves and an anonymous reviewer are thanked for their constructive reviews of the manuscript, and we thank journal editor, Toru Takeshita, for editorial guidance.

References

Ackermann, R.V., Schlische, R.W., 1997. Anticlustering of small normal faults around larger faults. Geology 25, 1127–1130.
Anderson, E.M., 1951. The Dynamics of Faulting and Dyke Formation with Applications to Britain. Oliver & Boyd, Edinburgh.
Badley, M., Price, J., Dahl, C.R., Agdestein, T., 1988. The structural evolution of the northern Viking Graben and its bearing upon extensional modes of basin formation. J. Geol. Soc. 145, 455–472.
Baudon, C., Cartwright, J., 2008. The kinematics of reactivation of normal faults using high resolution throw mapping. J. Struct. Geol. 30, 1072–1084.
Behn, M.D., Lin, J., Zuber, M.T., 2002. A continuum mechanics model for normal faulting using a strain rate softening rheology: implications for thermal and rheological controls on continental and oceanic rifting. Earth Planet. Sci. Lett. 202, 725–740.
Bellahsen, N., Fournier, M., d'Acremont, E., Leroy, S., Daniel, J., 2006. Fault reactivation and rift localization: Northeastern Gulf of Aden margin. Tectonics 25.
Childs, C., Watterson, J., Walsh, J.J., 1995. Fault overlap zones within developing normal fault systems. J. Geol. Soc. 152 (3), 535–549.
Childs, C., Nicol, A., Walsh, J.J., Watterson, J., 1996. Growth of vertically segmented normal faults. J. Struct. Geol. 18 (12), 1389–1397.
Cowie, P., Gupta, S., Dawers, N., 2000. Implications of fault array evolution for synrift depocentre development: insights from a numerical fault growth model. Basin Res. 12, 241–261.
Cowie, P., Roberts, G.P., 2001. Constraining slip rates and spacings for active normal faults. J. Struct. Geol. 23, 1901–1915.
Cowie, P.A., Scholz, C.H., 1992. Physical explanation for the displacement-length relationship of faults using a post-yield fracture mechanics model. J. Struct. Geol. 14 (10), 1133–1148.
Cowie, P.A., Underhill, J.R., Behn, M.D., Lin, J., Gill, C.E., 2005. Spatio-temporal evolution of strain accumulation derived from multi-scale observations of Late Jurassic rifting in the northern North Sea: a critical test of models for lithospheric extension. Earth Planet. Sci. Lett. 234, 401–419.
Cundall, P.A., Strack, O., 1979. A discrete numerical model for granular assemblies. Géotechnique 29, 47–65.
Dawers, N.H., Anders, M.H., Scholz, C.H., 1993. Fault length and displacement: scaling laws. Geology 21, 1107–1110.
Deng, C., Fossen, H., Gawthorpe, R.L., Rotevatn, A., Jackson, A.L., Fazlikhani, H., 2017. Influence of fault reactivation during multiphase rifting: the Oseberg area, Northern North Sea rift. Mar. Petrol. Geol. 86, 1252–1272.
Donzé, F., Mora, P., Magnier, S.-A., 1994. Numerical simulation of faults and shear zones. Geophys. J. Int. 116, 46–52.
Duffy, O.B., Bell, R.E., Jackson, C.A., Gawthorpe, R.L., Whipp, P.S., 2015. Fault growth and interactions in a multiphase rift fault network: Horda Platform, Norwegian North Sea. J. Struct. Geol. 80, 99–119.
Egholm, D.L., Sandiford, M., Clausen, O.R., Nielsen, S.B., 2007. A new strategy for discrete element numerical models: 2. sandbox applications. J. Geophys. Res. Solid Earth 112 (B5).
Finch, E., Gawthorpe, R., 2017. Growth and interaction of normal faults and fault network evolution in rifts: insights from three-dimensional discrete element modelling. Geol. Soc. Lond. Spec. Publ. SP439.23.
Finch, E., Hardy, S., Gawthorpe, R., 2003. Discrete element modelling of contractional fault-propagation folding above rigid basement fault blocks. J. Struct. Geol. 25 (4), 515–528.
Finch, E., Hardy, S., Gawthorpe, R., 2004. Discrete-element modelling of extensional fault-propagation folding above rigid basement fault blocks. Basin Res. 16 (4), 467–488.
Fossen, H., Rotevatn, A., 2016. Fault linkage and relay structures in extensional settings—a review. Earth Sci. Rev. 154, 14–28.
Færseth, R., 1996. Interaction of Permo-Triassic and Jurassic extensional fault-blocks during the development of the Northern North Sea. J. Geol. Soc. 153, 931–944.
Færseth, R.B., Knudsen, B.E., Liljedahl, T., Midbøe, P.S., Søderstrøm, B., 1997. Oblique rifting and sequential faulting in the Jurassic development of the Northern North Sea. J. Struct. Geol. 19, 1285–1302.
Frankowicz, E., McClay, K., 2010. Extensional fault segmentation and linkages, Bonaparte Basin, outer North west shelf, Australia. AAPG Bull. 94, 977–1010.
Gawthorpe, R., Leeder, M., 2000. Tectono-sedimentary evolution of active extensional basins. Basin Res. 12, 195–218.
Gawthorpe, R.L., Jackson, C.A.-L., Young, M.J., Sharp, I.R., Moustafa, A.R., Leppard, C.W., 2003. Normal fault growth, displacement localisation and the evolution of normal fault populations: the Hammam Faraun fault block, Suez rift, Egypt. J. Struct. Geol. 25, 883–895.
Giba, M., Walsh, J., Nicol, A., 2012. Segmentation and growth of an obliquely reactivated normal fault. J. Struct. Geol. 39, 253–267.
Gillespie, P.A., Walsh, J.T., Watterson, J., 1992. Limitations of dimension and displacement data from single faults and the consequences for data analysis and interpretation. J. Struct. Geol. 14 (10), 1157–1172.
Gupta, A., Scholz, C.H., 2000. A model of normal fault interaction based on observations and theory. J. Struct. Geol. 22, 865–879.
Hardy, S., Finch, E., 2005. Discrete-element modelling of detachment folding. Basin Res. 17, 507–520.
Hardy, S., Finch, E., 2006. Discrete element modelling of the influence of cover strength on basement-involved fault-propagation folding. Tectonophysics 415 (1), 225–238.
Hardy, S., Finch, E., 2007. Mechanical stratigraphy and the transition from trishear to kink-band fault-propagation fold forms above blind basement thrust faults: a discrete-element study. Mar. Pet. Geol. 24 (2), 75–90.
Hardy, S., 2013. Propagation of blind normal faults to the surface in basaltic sequences: insights from 2d discrete element modelling. Mar. Pet. Geol. 48 (2), 149–159.
Henza, A.A., Withjack, M.O., Schlische, R.W., 2010. Normal-fault development during two phases of non-coaxial extension: an experimental study. J. Struct. Geol. 32, 1656–1667.
Henza, A.A., Withjack, M.O., Schlische, R.W., 2011. How do the properties of a pre-existing normal-fault population influence fault development during a subsequent phase of extension? J. Struct. Geol. 33, 1312–1324.
Huismans, R.S., Beaumont, C., 2007. Roles of lithospheric strain softening and heterogeneity in determining the geometry of rifts and continental margins. In: In: Karner, G.D., Manatschal, G., Pinheiro, L.M. (Eds.), Imaging, Mapping and Modelling Continental Lithosphere Extension and Breakup, vol. 282. Geological Society, London, Special Publications, pp. 111–138.
Imber, J., Tuckwell, G.W., Childs, C., Walsh, J.J., Manzocchi, T., Heath, A.E., Bonson, C.G., Strand, J., 2004. Three-dimensional distinct element modelling of relay growth and breaching along normal faults. J. Struct. Geol. 26, 1897–1911.
Jackson, C.A.-L., Rotevatn, A., 2013. 3D seismic analysis of the structure and evolution of a salt-influenced normal fault zone: a test of competing fault growth models. J. Struct. Geol. 54, 215–234.
Keep, M., McClay, K., 1997. Analogue modelling of multiphase rift systems. Tectonophysics 273, 239–270.
Kim, Y.S., Sanderson, D.J., 2005. The relationship between displacement and length of faults: a review. Earth Sci. Rev. 68 (3), 317–334.
King, G.C.P., Stein, R.S., Rundle, J.B., 1988. The growth of geological structures by repeated earthquakes 1. Conceptual framework. J. Geophys. Res. 93 (11), 13307–13318.
Komoróczi, A., Abe, S., Ueai, J.L., 2013. Meshless numerical modelling of brittle-viscous deformation: first results on boudinage and hydrofracturing using a coupling of discrete element method (DEM) and smoothed particle hydrodynamics (SPH). Comput. Geosci. 17, 373–390.
Kusznir, N.J., Park, R.G., 1987. The extensional strength of the continental lithosphere: its dependence on geothermal gradient, and crustal composition and thickness. Geol. Soc. Lond. Spec. Publ. 28 (1), 35–52.
Lepvrier, C., Fournier, M., Bérard, T., Roger, J., 2002. Cenozoic extension in coastal Dhofar (southern Oman): implications on the oblique rifting of the Gulf of Aden. Tectonophysics 357, 279–293.
McClay, K., White, M., 1995. Analogue modelling of orthogonal and oblique rifting. Mar. Pet. Geol. 12, 137–151.
McLeod, A., Dawers, N.H., Underhill, J.R., 2000. The propagation and linkage of normal faults: insights from the Strathspey-Brent-Statfjord fault array, Northern North Sea. Basin Res. 12, 263–284.
Meyer, V., Nicol, A., Childs, C., Walsh, J., Watterson, J., 2002. Progressive localisation of strain during the evolution of a normal fault population. J. Struct. Geol. 24, 1215–1231.
Mora, P., Place, D., 1993. A lattice solid model for the non-linear dynamics of earthquakes. Int. J. Mod. Phys. C4, 1059–1074.
Mora, P., Place, D., 1994. Simulation of the frictional stick-slip instability. Pure Appl. Geophys. 143, 61–87.
Mora, P., Place, D., 1998. Numerical simulation of earthquake faults with gouge: toward a comprehensive explanation for the heat flow paradox. J. Geophys. Res. Solid Earth 103 (B9), 21067–21089.
Morley, C., Gabdi, S., Seusutthiya, K., 2007. Fault superimposition and linkage resulting from stress changes during rifting: examples from 3D seismic data, Phitsanulok Basin, Thailand. J. Struct. Geol. 29, 646–663.
Morley, C., Haranya, C., Phoosongsee, W., Pongwapee, S., Kornsawan, A., Wonganan, N., 2004. Activation of rift oblique and rift parallel pre-existing fabrics during extension and their effect on deformation style: examples from the rifts of Thailand. J. Struct. Geol. 26, 1803–1829.
Nicol, A., Walsh, J.J., Watterson, J., Underhill, J.R., 1997. Displacement rates of normal faults. Nature 390 (6656), 157–159.
Nixon, C.W., Sanderson, D.J., Dee, S.J., Bull, J.M., Humphreys, R.J., Swanson, M.H., 2014. Fault interactions and reactivation within a normal-fault network at Milne Point, Alaska. AAPG Bull. 98 (10), 2081–2107.
Odinsen, T., Reemst, P., Beek, P.V.D., Faleide, J.I., Gabrielsen, R.H., 2000. Permo-Triassic and Jurassic extension in the northern North Sea: results from tectonostratigraphic forward modelling. Geol. Soc. Lond. Spec. Publ. 167, 83–103.
Ranalli, G., 1995. Rheology of the Earth, second ed. Chapman and Hall, London.
Schlische, R.W., Young, S.S., Ackermann, R.V., Gupta, A., 1996. Geometry and scaling

relations of a population of very small rift-related normal faults. Geology 24 (8), 683–686.
Schöpfer, M.P.J., Childs, C., Walsh, J.J., 2006. Localisation of normal faults in multilayer sequences. J. Struct. Geol. 28 (5), 816–833.
Schöpfer, M.P.J., Childs, C., Walsh, J.J., 2007a. Two-dimensional distinct element modeling of the structure and growth of normal faults in multilayer sequences: 1. model calibration, boundary conditions, and selected results. J. Geophys. Res. Solid Earth 112 (B10), 1–8.
Schöpfer, M.P.J., Childs, C., Walsh, J.J., 2007b. 2d distinct element modeling of the structure and growth of normal faults in multilayer sequences: 2. impact of confining pressure and strength contrast on fault zone growth and geometry. J. Geophys. Res. Atmos. 112 (B10), 1–8.
Soliva, R., Benedicto, A., Maerten, L., 2006. Spacing and linkage of confined normal faults: importance of mechanical thickness. J. Geophys. Res. 111 (B1), 17.
Walsh, J.J., Childs, C., et al., 2001. Geometric controls on the evolution of normal fault systems. In: In: Holdsworth, R.E., Strachan, R.A., Magloughlin, J.F., Knipe, R.J. (Eds.), The Nature and Tectonic Significance of Fault Zone Weakening, vol. 186. Geological Society, London, Special Publications, pp. 157–169.
Walsh, J., Nicol, A., Childs, C., 2002. An alternative model for the growth of faults. J. Struct. Geol. 24, 1669–1675.
Walsh, J.J., Bailey, W.R., Childs, C., Nicol, A., Bonson, C.G., 2003. Formation of segmented normal faults: a 3-D perspective. J. Struct. Geol. 25 (8), 1251–1262.
Walsh, J.J., Watterson, J., 1988. Analysis of the relationship between displacements and dimensions of faults. J. Struct. Geol. 10 (3), 239–247.
Wenk, L., Huhn, K., 2013. The influence of an embedded viscoelastic–plastic layer on kinematics and mass transport pattern within accretionary wedges. Tectonophysics 608, 653–666.
Whipp, P., Jackson, C., Gawthorpe, R., Dreyer, T., Quinn, D., 2014. Normal fault array evolution above a reactivated rift fabric; a subsurface example from the northern Horda Platform, Norwegian North Sea. Basin Res. 26, 523–549.
Willemse, E.J.M., Pollard, D.D., Aydin, A., 1996. Three-dimensional analyses of slip distributions on normal fault arrays with consequences for fault scaling. J. Struct. Geol. 18, 295–309.